Figure 1. In vitro alkaline phosphatase activity (ALP) of fully open interconnected porous calcium hydroxyapatite (IP-CHA), which was combined with MMCs and cultured in the presence or absence of dexamethasone (Dex). Two types of IP-CHA, one with pores with an average diameter of 150 μm (HA150) and the other with pores with an average diameter of 300 μm (HA300), were used in this experiment as in vitro cell culture substrata. The culture was performed with or without Dex. ALP activity of four groups: HA150/MMCs with Dex, HA300/MMCs with Dex, HA150/MMCs without Dex, and HA300/MMCs without Dex. Data are presented as mean ± SD (n = 5). **$p < 0.01$ vs. HA150/MMCs with Dex. All ALP activity in HA150/MMCs and HA300/MMCs without Dex was significantly lower than that of HA150/MMCs with Dex.

confirmed that both types of IP-CHA can maintain Dex-dependent in vitro osteoblastic differentiation of MMCs, and HA150 has more superior capabilities for supporting differentiation than does HA300.

Histological Analyses After In Vivo Implantation

As stated above, HA150/MMCs and HA300/MMCs can show in vitro osteoblastic differentiation under the culture condition with Dex. We also reported that the ceramic/MMCs cultured with Dex showed immediate and more copious new bone formation after in vivo implantation compared with those cultured without Dex. Therefore, we performed in vivo implantation using ceramics that were combined with MMCs and cultured for 2 weeks with Dex. After the 2-week culture, the pore surface of the ceramics could be covered with a thin layer of bone matrix together with a lining of active osteoblasts and thus we refer to these cultured ceramics as constructs (ceramics/MMCs/cult construct). As a negative control, we also implanted the ceramics without cells.

Two weeks after in vivo implantation of HA150/MMCs/cult and HA300/MMCs/cult, we were able to detect obvious bone formation in many pore areas of the ceramic (Fig. 2). Bone tissue, together with many cuboidal active osteoblasts, was observed in contact with the pore surface. Newly formed vascular vessels were also observed in some pores. This finding suggests that a

capillary network had been established in the IP-CHA because of the sufficient interpore connections of the ceramics. At 8 weeks after implantation (Fig. 3A, B), the bone areas and number of osteocytes in the bone matrix increased and almost all pore areas showed bone formation. In addition, regenerated bone marrow was observed together with fat cells in many pores (Fig. 3A, B). These findings indicate the importance of porous architecture (excellent interpore connections) of IP-CHA for new bone formation. To confirm the importance of the interpore connections, we also utilized three commercially available Japanese synthetic porous hydroxyapatite ceramics (HA-A, HA-B, and HA-C). The porous architectures of these ceramics are different from IP-CHA: each pore of the commercial ceramics is not fully interconnected and have many isolated porous areas or dead-end pores. These three ceramics (HA-A, HA-B, and HA-C) were combined with MMCs and cultured with Dex for 2 weeks to make constructs of HA-A/MMCs/cult, HA-B/MMCs/cult, and HA-C/MMCs/cult. These constructs were implanted at subcutaneous sites for 8 weeks and harvested. The culture/implantation methods were the same as those applied for the constructs of HA150/MMCs/cult and HA300/MMCs/cult. In contrast to IP-CHA (Fig. 3A, B), only a few pore areas in these constructs showed newly formed bone (Fig. 3C–E). Furthermore, some pore areas did not show any newly formed tissue and were empty. Therefore, ceramics having full interpore connections (HA150 and HA300) cultured with MMCs have superior in vivo bone-forming capabilities in comparison with other ceramics (HA-A, HA-B, and HA-C) with MMCs.

Although the constructs of HA150/MMCs/cult and HA300/MMCs/cult had excellent osteogenic properties, the ceramics not combined with the cells formed only fibrovascular tissue and there was no evidence of bone formation in the pore areas of the ceramics (Fig. 4).

Biochemical Analyses After In Vivo Implantation

Histological analyses showed the in vivo osteogenic capacity of the constructs of HA150/MMCs/cult and HA-300/MMCs/cult and nonosteogenic capacity of the IP-CHA (HA150 and HA300) without MMCs. To demonstrate the quantitative analyses of the osteogenic capacity, we measured ALP activity as well as the osteocalcin contents of the implants, because ALP is known to localize on the cellular membrane of active osteoblasts and osteocalcin is the bone-specific protein produced exclusively by osteoblasts.

High levels of ALP activities could be detected in both the constructs of HA150/MMCs/cult and HA300/MMCs/cult. Both showed a peak in activity 2 weeks after implantation followed by a decrease. However, the levels of activity in HA150/MMCs/cult at 4 and 6 weeks

out MMCs were also implanted as controls. The rats were sacrificed at 2, 4, 6, and 8 weeks after implantation, and the implants were harvested from each experimental group for biochemical and histological assay. All procedures used in the animal experiments complied with the standards given in the Osaka University Medical School Guidelines for the Care and Use of Laboratory Animals.

Histological Examination

To obtain decalcified sections, 5 implants harvested from each group at 2, 4, 6, and 8 weeks were fixed in 10% buffered formalin, decalcified with K-CX solution (Falma Co., Tokyo, Japan), and embedded in paraffin. They were cut parallel to the round face of the implants and were stained with hematoxylin and eosin for light microscopy.

Biochemical Analysis

ALP activity was measured as reported previously (24). Each ceramic disk was crushed, homogenized in 0.2% Nonidet P-40 containing 1 mM $MgCl_2$, and centrifuged at 10,000 rpm for 1 min at 4°C. Then the supernatant was assayed for ALP using p-nitrophenyl phosphate as a substrate. ALP activity was represented as µmol of p-nitrophenol released per ceramic disk for 30 min of incubation at 37°C (19).

Osteocalcin was extracted from the sediment after extraction of 20% formic acid for 2 weeks at 4°C. An aliquot (1 ml) of the formic acid extract was then applied to a column of NAP-10 (Sephadex G-25 DNA grade, Amersham Bioscience, Uppsala, Sweden) and was eluted with 1.5 ml of 10% formic acid. Protein fractions were collected, lyophilized, and prepared for the assay of intact rat osteocalcin as previously described (6). The assay method (Rat Osteocalcin EIA Kit; No. BT-490 Biomedical Technologies Inc., Stoughton, MA) utilized two antibodies that recognized the N-and C-terminal amino acid regions of rat osteocalcin. Purified rat osteocalcin was used for standard and tracer.

Microcomputed Tomography Evaluation

Bone formed in the pore areas of the ceramics was evaluated by microcomputed tomography [micro-CT: MCT-CB100MF(Z); Hitachi Medical Corporation, Tokyo, Japan]. After fixation in 10% buffered formalin, each implant was placed as a round face facing the jig surface and scanned at intervals of every 10 µm at a voltage of 50 kV, 200 µA. The analytical condition was superprecision mode and 7× magnification with an image intensifier field of 1.8 in. After the samples were scanned, they were decalcified and prepared for the histological sections. The micro-CT image at almost the same level as the histological section was compared and the intensity

of the newly formed bone in the micro-CT image was determined. Then the newly formed bone areas in the micro-CT images that matched with the histology were extracted and their volumes were measured using the software package, TRI3D-BON (Ratoc System Engineering Co., Ltd., Tokyo, Japan).

Statistical Analysis

Statistical analysis was performed using unpaired t-test with statistical analysis software, STATVIEW version 4.5 (SAS Institute Inc., Cary, NC). The statistical significance level was set at $p = 0.05$.

RESULTS

Evaluation of Interconnected Porosity

The distribution of the interpore connections was measured using mercury porosimetry technique. In IP-CHA, most of the interpore connections ranged from 10 to 100 µm in diameter, a dimension that theoretically would be permissive to cell migration or tissue invasion from pore to pore. The interpore connections of HA150 and HA300 had a maximum peak at 40 and 80 µm, respectively. Interpore connections >10 µm accounted for as much as 90% of the total porosities in IP-CHA. The available porosities of HA150 and HA300 were as high as 67% and 70%, respectively. However, in HA-A, HA-B, and HA-C, the maximum peaks of the interpore connections were at 22, 15, and <1 µm, respectively. In addition, the total number of the interpore connections was much less than IP-CHA. The available porosities of HA-A, HA-B, and HA-C were as low as 28.5%, 36.7%, and 2.5%.

### In Vitro Osteoblastic Differentiation of MMCs

It is well known that MMCs can differentiate into osteoblasts in culture conditions with Dex (9,15). We also reported that in vitro osteoblastic differentiation can occur on the surface of many kinds of ceramics (16,17). As a result of these findings, we first examined whether the fully open interconnected porous calcium hydroxyapatite ceramics (IP-CHA) can support in vitro differentiation by measuring ALP, one of the osteoblastic markers. IP-CHA (HA150 and HA300), having two different pore sizes, were combined with MMCs and then cultured for 2 weeks in the presence or absence of Dex. As shown in Figure 1, the ALP activities of HA150 with MMCs (HA150/MMCs) and that of HA300 with MMCs (HA300/MMCs) cultured with Dex were considerably higher than those cultured without Dex throughout the culture period. The fluctuation of ALP activities of HA150/MMCs and HA300/MMCs with Dex during the culture period showed a similar pattern, but the activity of HA150/MMCs was higher than that of HA300/MMCs at 4 and 14 days after culture. These findings
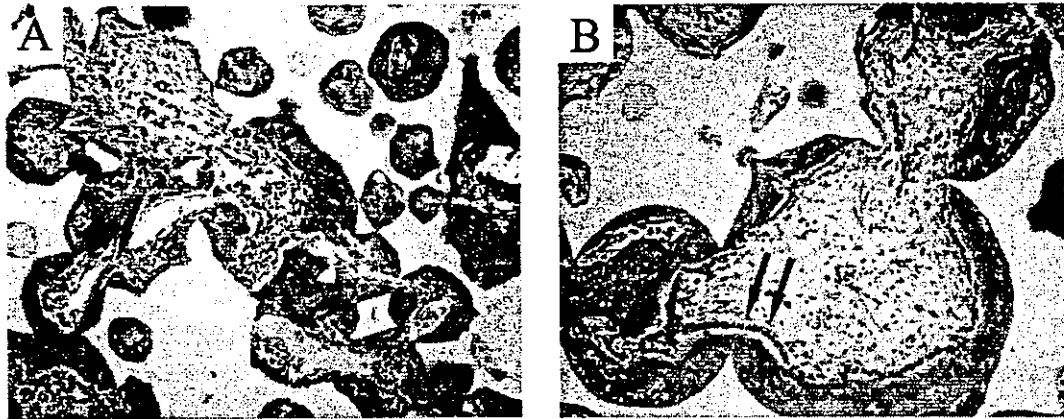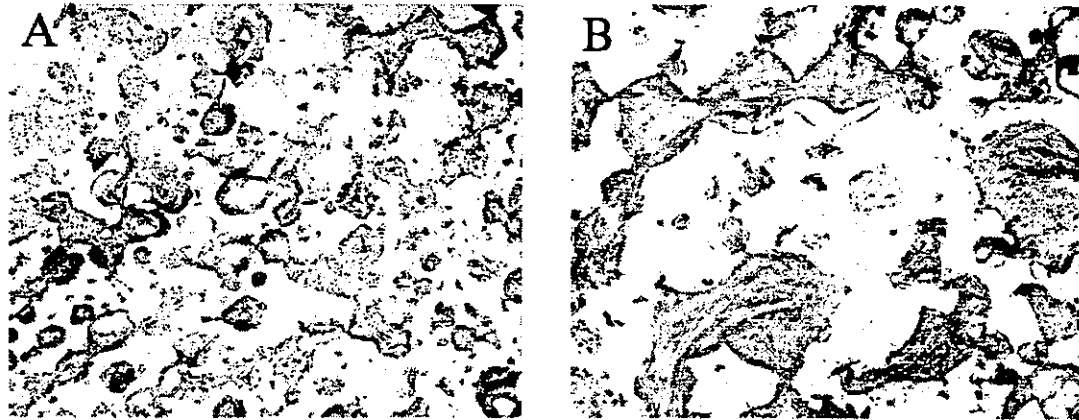
Figure 2. Histology of 2-week in vivo implanted IP-CHA construct, which was combined with MMCs and cultured with Dex. (A) The HA150/MMCs/cult construct and (B) HA300/MMCs/cult construct 2 weeks after implantation. The white area is the ghost of hydroxyapatite ceramic produced by decalcification; the black area is the bone formed in the ceramic pore areas. The arrows indicate active osteoblasts forming bone. Hematoxylin and eosin staining; original magnification ×100.

after implantation were higher than those in HA300/MMCs/cult (Fig. 5). Thus, the decrease was more evident in HA300/MMCs/cult than in HA150/MMCs/cult. The osteocalcin contents could be detected at 2 weeks

after implantation of both constructs, followed by a steady increase over time. During this time, the contents of osteocalcin in HA150/MMCs/cult were always significantly higher than in HA300/MMCs/cult (Fig. 6). In
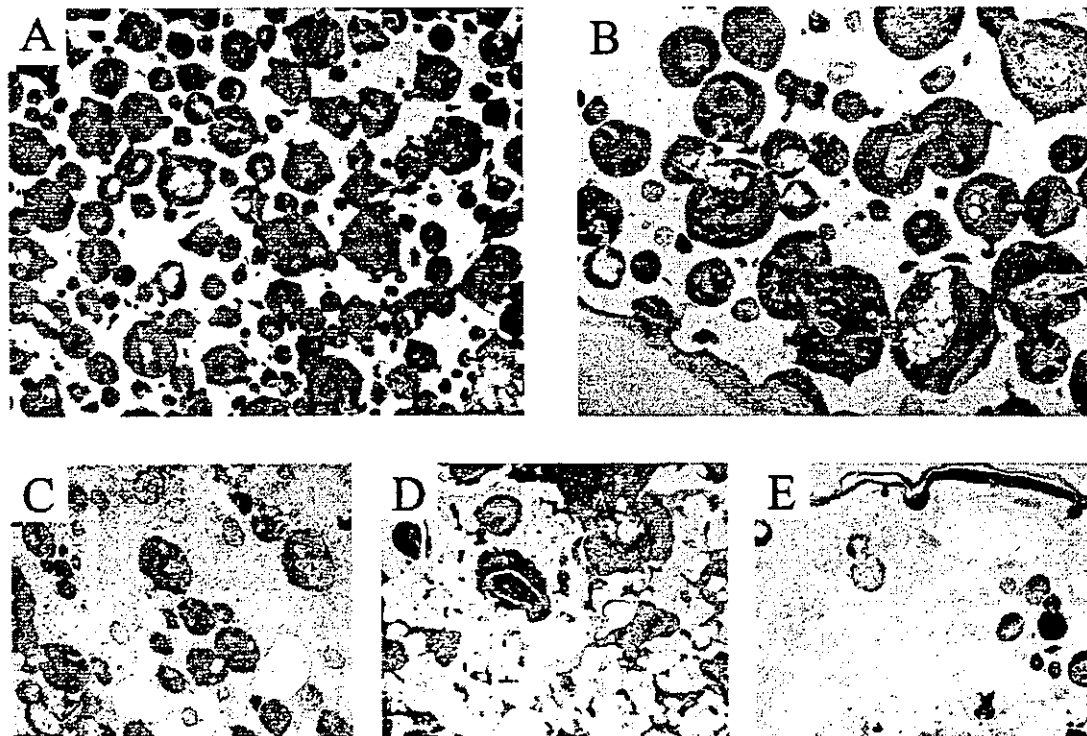

Figure 3. Histology of 8-week in vivo implant of various ceramic constructs combined with MMCs and cultured with Dex. (A) HA150/MMCs/cult, (B) HA300/MMCs/cult, (C) HA-A/MMCs/cult, (D) HA-B/MMCs/cult, (E) HA-C/MMCs/cult 8 weeks after implantation. The white area is the ghost of hydroxyapatite ceramic produced by decalcification; the black area is the bone formed in the ceramic pore areas. The HA-A/MMCs/cult, HA-B/MMCs/cult, and HA-C/MMCs/cult showed less bone formation in the pore areas compared with HA150/MMCs/cult and HA300/MMCs/cult. Hematoxylin and eosin staining; original magnification ×40.

Figure 4. Histology of 8-week in vivo implanted IP-CHA without cells. (A) HA150 without cells and (B) HA300 without cells 8 weeks after implantation. In contrast to Figures 2 and 3, the IP-CHA ceramics do not show any bone formation. Hematoxylin and eosin staining; original magnification ×40.

contrast, the ALP activity and osteocalcin contents in the HA150 and HA300 without marrow cells were at basal levels. All of these results confirmed the osteogenic capacity of the constructs of IP-CHA cultured with MMCs. We used two different IP-CHA having two different pore sizes (i.e., HA150 and HA300 had mean pore diameters of 150 and 300 μm, respectively). The ALP and osteocalcin contents of HA150 combined with MMCs were more than those of HA300, meaning that HA150 had superior in vivo osteogenic capacity to that of HA300.
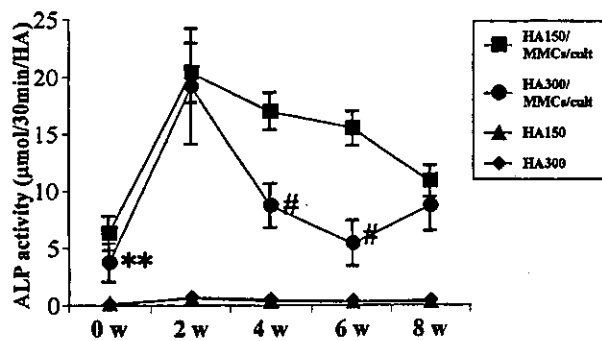

Figure 5. In vivo alkaline phosphatase (ALP) activities of implanted HA150/MMCs/cult, HA300/MMCs/cult, HA150, and HA300. IP-CHA was combined with MMCs and cultured with Dex for 2 weeks (HA150/MMCs/cult and HA300/MMCs/cult), then implanted and harvested 0–8 weeks after implantation. HA150 and HA300 without cells were also implanted as controls. The implants were used for ALP assay as described in Materials and Methods. Data are presented as mean ± SD ($n = 5$). **$p < 0.01$, #$p < 0.0001$ vs. HA150/MMCs/cult. All ALP activities in HA150 and HA300 were significantly lower than those of HA150/MMCs/cult.

Micro-CT Evaluation of Newly Formed Bone Volume

To measure the total bone volume in the constructs of IP-CHA (HA150/MMCs/cult and HA300/MMCs/cult) after in vivo implantation, we studied the micro-CT analysis. Figure 7A shows a histological section of the HA300/MMCs/cult construct 8 weeks after implantation; Figure 7B shows a micro-CT image at almost the same level of the histological section of the construct. The micro-CT images show areas having high (white), middle (gray), and low (black) intensities. After matching the histological section with the micro-CT image, we defined the white, gray, and black areas as IP-CHA (HA), newly formed bone (NB), and fibrovascular tissue with fat cells (F), respectively. The software, TRI3D-BON, turned the newly formed bone areas in Figure 7B,
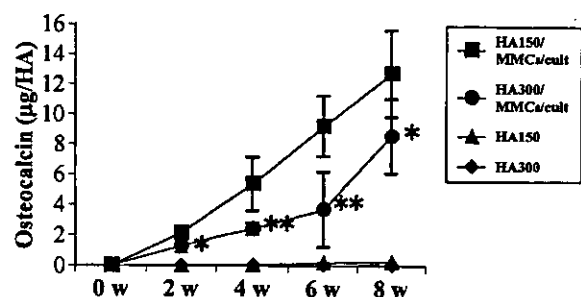
Figure 6. Osteocalcin contents of implanted HA150/MMCs/cult, HA300/MMCs/cult, HA150, and HA300. Details of the implants are described in the legend to Figure 5. The implants were used for measuring the osteocalcin contents as described in Materials and Methods. Data are presented as mean ± SD ($n = 5$). *$p < 0.05$, **$p < 0.01$ vs. HA150/MMCs/cult. All osteocalcin contents in HA150 and HA300 were significantly lower than those of HA150/MMCs/cult.
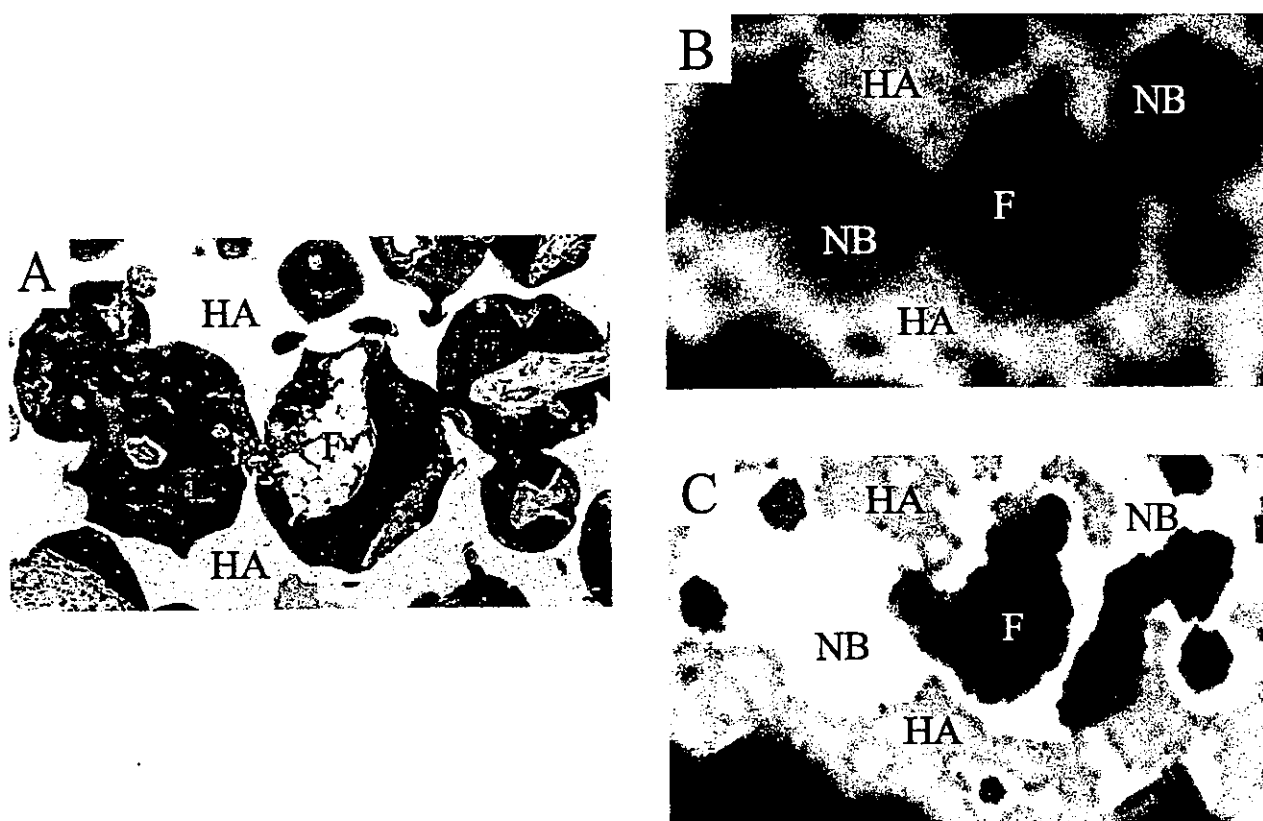
Figure 7. Micro-CT evaluation of newly formed bone in IP-CHA. (A) Histological section of HA300/MMCs/cult construct 8 weeks after implantation. Hematoxylin and eosin staining; original magnification ×100. (B) Micro-CT image at almost the same level of the histological section of the construct. (C) Same image of (B) except the gray-colored areas (newly formed bone) are represented in yellow. The micro-CT image (B) depicts the areas having a high (white), middle (gray), and low (black) intensity. By matching the image with the histological section (A), we defined the white, gray, and black areas as IP-CHA (HA), newly formed bone (NB), and soft fibrous tissue including vasculature and fat (F), respectively. Newly formed bone areas in (B) represented as gray areas were turned into yellow by the software program, TRI3D-BON, and illustrated in (C).

represented by the gray areas, into yellow, as shown in Figure 7C. We used the program to measure the yellow areas in each micro-CT section and finally calculated the total volume of yellow-colored areas, which was defined as the total volume of newly formed bone in the constructs. The yellow-colored newly formed bone in HA150/MMCs/cult and HA300/MMCs/cult could be detected 2 weeks after implantation. The bone volumes in both HA150/MMCs/cult and HA300/MMCs/cult gradually increased over time (Fig. 8). We also assembled a three-dimensional (3D) image and evaluated the distribution of newly formed bone at the sagittal section around the center of HA150/MMCs/cult and HA300/MMCs/cult 8 weeks after implantation. As shown in Figure 9, extensive newly formed bone is evident not only in the surface pore areas but also in the center pore areas in both constructs.

The newly formed bone volumes were also measured in the constructs using commercially available synthetic porous hydroxyapatite ceramics (HA-A/MMCs/cult, HA-

B/MMCs/cult, and HA-C/MMCs/cult) 8 weeks after implantation. The volumes of these constructs were less than those of HA150/MMCs/cult and HA300/MMCs/cult (Table 1). These data confirmed the histological analyses shown in Figure 3.

DISCUSSION

The present results confirmed the outstanding role played by IP-CHA in supporting in vitro osteoblastic differentiation of marrow mesenchymal cells (MMCs). More importantly, the ceramics having the cultured cells (MMCs/ceramic/cult constructs) can induce new bone formation after in vivo implantation. Therefore, the constructs having osteogenic capability can be applied in massive bone defects or other cases where there is inferior repair capacity. Thus, the tissue engineering approach is very useful for the regeneration of hard tissue. This approach requires a porous scaffold to make the construct. The scaffold should be biocompatible and have sufficient initial mechanical strength to support the
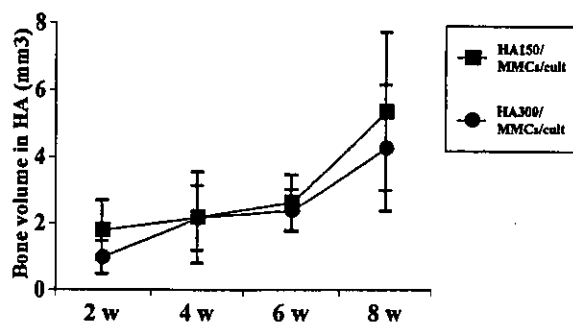
Figure 8. Bone volumes in IP-CHA determined by Micro-CT analysis. Temporal changes in bone volumes in HA150/MMCs/cult and HA300/MMCs/cult after implantation. Using the software, TRI3D-BON, we measured the yellow areas in each micro-CT section (Fig. 7C) and finally calculated the total volume of yellow, which was defined as the total volume of the newly formed bone in the constructs. The yellow-colored newly formed bone in HA150/MMCs/cult and HA300/MMCs/cult could be detected 2 weeks after implantation. The bone volumes in both HA150/MMCs/cult and HA300/MMCs/cult gradually increase with the passage of implantation time. There was no significant difference between these two constructs. Data are presented as mean $\pm$ SD ($n = 5$).

skeletal structure under weight-bearing conditions. In addition, the scaffold must have a 3D interconnected porous structure to introduce MMCs into the center of the scaffold. The MMCs should differentiate into the osteoblastic lineage.

As we have stated, an interconnected porous structure is very important in the tissue engineering approach. However, currently available commercial synthetic porous ceramics do not possess the ideal interconnected porous structure. To prove the necessity of a porous structure in supporting osteoblastic differentiation, we analyzed the in vivo bone-forming capability of porous ceramics/MMCs constructs by two different morphological approaches: the traditional histological approach and micro-CT analysis. The histological analysis is based on 2D findings of the cut section, and the extent of the bone formation areas may not accurately reflect the bone volume of the constructs because the areas depend on the cutting levels of the sample. In this regard, micro-CT can reconstruct the 3D structure of the HA ceramics, evaluate the 3D distribution of the newly formed bone, and, finally, calculate the bone volume in the ceramics. What is also important is that the analyzed samples can further be utilized for ordinal histological analysis.

As shown in the histological findings of Figures 2 and 3, the constructs of HA-A/MMCs/cult, HA-B/MMCs/cult, and HA-C/MMCs/cult showed new bone formation only in the restricted porous area near the ceramics' surface. In general, as the porosity of porous HA ceramics is higher, the interpore connection rate be-

comes high. However, to allow cell migration or tissue invasion from pore to pore, theoretically the diameter of the interconnection requires at least 10 μm. In this study, we measured the interpore connection of hydroxyapatite ceramics. Even highly porotic HA-B (70%) have limited interconnections of sufficient size (>10 μm) and the available porosity was as low as 36.7%. This limited interconnection may explain the poor new bone formation by the constructs using porous HA ceramics. In contrast, although the total porosity of IP-CHA was similar to HA-B, the interpore connections of IP-CHA were well controlled between 10 and 100 μm in diameter and the available porosity was from 67% to 70%. The constructs of HA150/MMCs/cult and HA300/MMCs/cult showed extensive bone formation in most pore areas regardless of location (i.e., the bone appeared in both the surface and center pore areas). This uniform appearance of the newly formed bone in most pore areas of the fully open IP-CHA is also revealed by micro-CT analysis. As shown in Figure 9, at the sagittal section of these constructs, excellent bone formation was seen at both the surface and center pore areas. Quantitative micro-CT analysis of bone formed in all constructs showed more bone formation in the HA150/MMCs/cult and HA300/MMCs/cult constructs than in other constructs (Table 1). These two different morphological analyses confirmed that IP-CHA is useful in the tissue engineering approach using MMCs, probably due to its well-organized interconnected porous structure.

The porous structure of IP-CHA was produced by a "foam-gel" technique using a cross-linking polyethyleneimine, enabling control of the pore size and porosity of IP-CHA. In the engineering of bone tissue, the ideal pore size is not clear, although some experiments suggest that a pore size of 200–400 μm is optimal for bone ingrowth (2,5,23). In this study, we used two different pore sizes of IP-CHA: HA150 with a mean pore diameter of 150 μm and HA300 with a mean diameter of 300 μm. Both HA150 and HA300 had the same porosity of 75%. As far as the mechanical properties are concerned, HA150 was superior to HA300 because the compressive strength of HA150 (10 MPa) is higher than that of HA300 (4 MPa) (unpublished data). Therefore, HA150 may be suitable material for bone reconstruction surgery, especially application in weight-bearing areas. An important question that remains, however, is whether the relatively small pore diameter of HA150 can support the osteogenic differentiation of MMCs. To address this point, we measured the level of ALP activity, the early marker of osteoblast differentiation, during in vitro culturing of MMCs in both HA150 and HA300. Both showed high levels of ALP activity with slightly higher levels of HA150 (Fig. 1). We also implanted these ceramics after culturing them with MMCs in Dex for 2 weeks (ceramics/MMCs/cult constructs) and measured
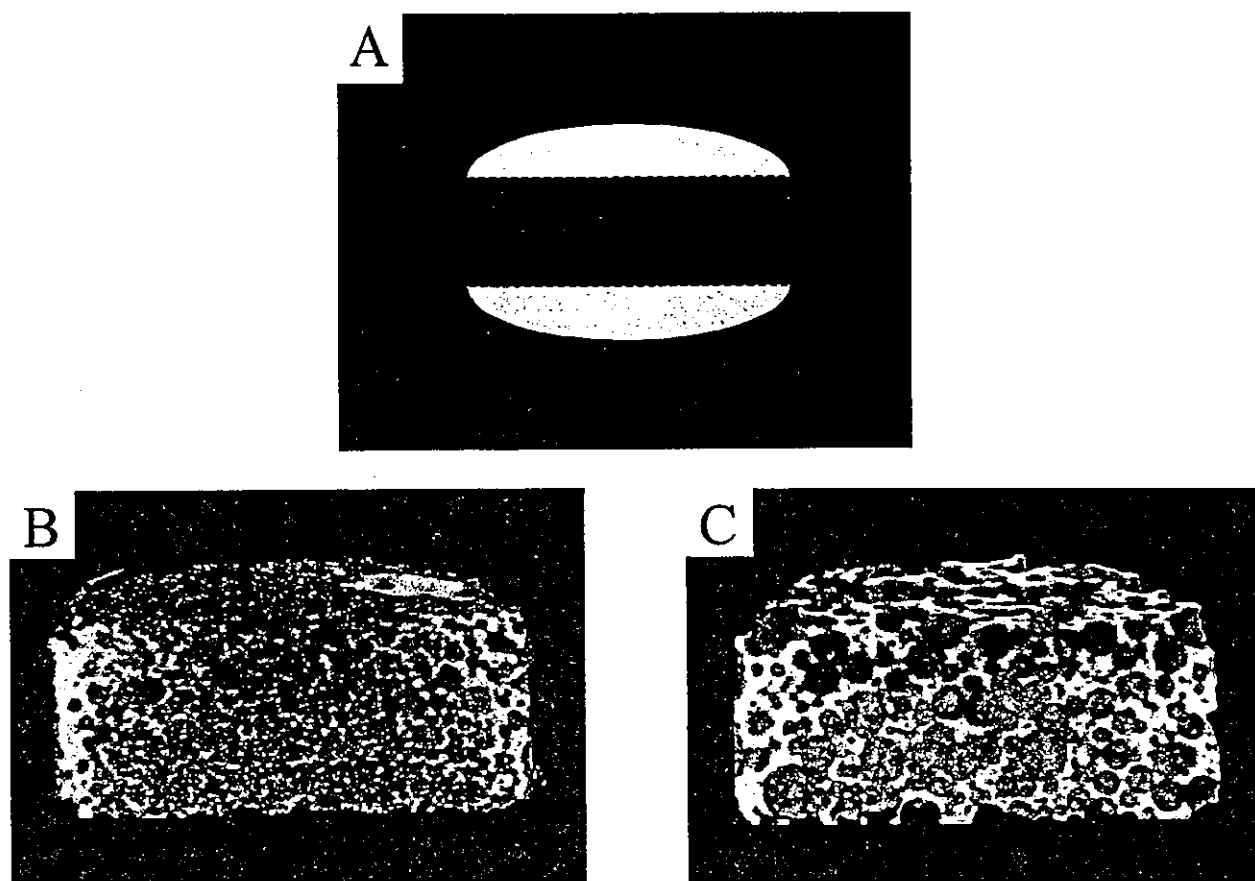
Figure 9. Three-dimensional distribution of newly formed bone in IP-CHA determined by Micro-CT analysis. (A) Illustration of the IP-CHA implant. The shaded area is the cross section of the implants. Three-dimensional micro-CT images at the cross section of the HA150/MMCs/cult (B) and HA300/MMCs/cult (C) 8 weeks after implantation. The three-dimensional (3D) image was constructed using the software, TRI3D-BON. The newly formed bone, originally represented in gray, now represented by orange.

the level of ALP activity and osteocalcin contents. Both the ALP activity and the osteocalcin contents of HA150/MMCs/cult were higher than those of HA300/MMCs/cult (Figs. 5 and 6). Micro-CT analysis also confirmed the comparable bone-forming capability of HA150/

Table 1. Bone Volumes of Various Constructs Determined by Micro-CT Analysis

	Bone Volume in Pore Areas (mm^3)
HA150/MMCs/cult ($n = 5$)	5.35 ± 2.36
HA300/MMCs/cult ($n = 5$)	4.26 ± 1.90
HA-A/MMCs/cult ($n = 5$)	1.88 ± 0.89*
HA-B/MMCs/cult ($n = 5$)	1.57 ± 0.60†
HA-C/MMCs/cult ($n = 5$)	0.52 ± 0.30†

Values are shown as mean ± SD. n: number of implants. There was no statistical difference between HA150/MMCs/cult and HA300/MMCs/cult.
*$p < 0.05$ vs. HA150/MMCs/cult and HA300/MMCs/cult.
†$p < 0.01$ vs. HA150/MMCs/cult and HA300/MMCs/cult.

MMCs/cult to that of HA300/MMCs/cult (Fig. 9, Table 1). These results demonstrated that HA150 with a pore diameter of 150 μm can support the osteoblastic differentiation of MMCs and that the HA150/MMCs construct has more extensive bone-forming capability than does the HA300/MMCs/cult construct. Because of the high degree of mechanical properties of HA150, the HA150/MMCs/cult construct seems to be an ideal tool in bone reconstruction surgery.

CONCLUSIONS

IP-CHA is an excellent ceramic for use in bone tissue engineering because of its fully interconnected porous structure, which allows MMC dispersion and supports their osteogenic differentiation. Ceramics having pores with an average diameter of 150 μm, average interconnecting pore diameter of 40 μm, and 75% porosity (HA150) have a high level of mechanical strength. When cultured with MMCs for 2 weeks in vitamin C, glycerophosphate, and dexamethasone, HA150 has extensive in vivo capability for forming new bone. There-

fore, in combination with MMCs culture, HA150 could be an extremely useful tissue engineering material in bone reconstruction surgery.

REFERENCES

1. Ayers, R. A.; Simske, S. J.; Nunes, C. R.; Wolford, L. M. Long-term bone ingrowth and residual microhardness of porous block hydroxyapatite implants in humans. J. Oral Maxillofac. Surg. 56:1297–1301; 1998.

2. Boyan, B. D.; Hummert, T. W.; Dean, D. D.; Schwartz, Z. Role of material surfaces in regulating bone and cartilage cell response. Biomaterials 17:137–146; 1996.

3. Bucholz, R.; Carlton, A.; Holmes, R. Interporous hydroxyapatite as a bone graft substitute in tibial plateau fractures. Clin. Orthop. 240:53–62; 1988.

4. de Groot, K. Bioceramic consisting of calcium phosphate salts. Biomaterials 1:47–50; 1980.

5. Dennis, J. E.; Haynesworth, S. E.; Young, R. G.; Caplan, A. I. Osteogenesis in marrow-derived mesenchymal cell porous ceramic composites transplanted subcutaneously: Effect of fibronectin and laminin on cell retention and rate of osteogenic expression. Cell Transplant. 1:23–32; 1992.

6. Dohi, Y.; Ohgushi, H.; Tabata, S.; Yoshikawa, T.; Dohi, K.; Moriyama, T. Osteogenesis associated with bone Gla protein gene expression in diffusion chambers by bone marrow cells with demineralized bone matrix. J. Bone Miner. Res. 7:1173–1180; 1992.

7. Jarcho, M. Calcium phosphate ceramics as hard tissue prosthetics. Clin. Orthop. 157:259–278; 1981.

8. Kato, K.; Aoki, H.; Tabata, T.; Ogiso, M. Biocompatibility of apatite ceramics in mandibles. Biomater. Med. Devices Artif. Organs 7:291–297; 1979.

9. Maniatopoulos, C.; Sodek, J.; Melcher, A. H. Bone formation in vitro by stromal cells obtained from marrow of young adult rats. Cell Tissue Res. 254:317–330; 1988.

10. Nakano, K.; Harata, S.; Suetsuna, F.; Araki, T.; Itoh, J. Spinous process-splitting laminoplasty using hydroxyapatite spinous process spacer. Spine 17:S41–S43; 1992.

11. Ohgushi, H.; Goldberg, V. M.; Caplan, A. I. Heterotopic osteogenesis in porous ceramics induced by marrow cells. J. Orthop. Res. 7:568–578; 1989.

12. Ohgushi, H.; Goldberg, V. M.; Caplan, A. I. Repair of bone defects with marrow and porous ceramic. Acta Orthop. Scand. 60:334–339; 1989.

13. Ohgushi, H.; Okumura, M. Osteogenic capacity of rat and human marrow cells in porous ceramics. Acta Orthop. Scand. 61:431–434; 1990.

14. Ohgushi, H.; Dohi, Y.; Tamai, S.; Tabata, S. Osteogenic differentiation of marrow stromal stem cells in porous hydroxyapatite ceramics. J. Biomed. Mater. Res. 27:1401–1407; 1993.

15. Ohgushi, H.; Dohi, Y.; Katuda, T.; Tamai, S.; Tabata, S.; Suwa, Y. In vitro bone formation by rat marrow cell culture. J. Biomed. Mater. Res. 32:333–340; 1996.

16. Ohgushi, H.; Dohi, Y.; Yoshikawa, T.; Tamai, S.; Tabata, S.; Okunaga, K.; Shibuya, T. Osteogenic differentiation of cultured marrow stromal stem cells on the surface of bioactive glass ceramics. J. Biomed. Mater. Res. 32:341–348; 1996.

17. Ohgushi, H.; Yoshikawa, T.; Nakajima, H.; Tamai, S.; Dohi, Y.; Okunaga, K. Al2O3 doped apatite-wollastonite containing glass ceramic provokes osteogenic differentiation of marrow stromal stem cells. J. Biomed. Mater. Res. 44:381–388; 1999.

18. Ohgushi, H.; Caplan, A. I. Stem cell technology and bioceramics: From cell to gene engineering. J. Biomed. Mater. Res. 48:–913–927; 1999.

19. Reddi, A. H.; Sullivan, N. S. Matrix-induced endochondral bone differentiation: Influence of hypophysectomy, growth hormone, and thyroid-stimulating hormone. Endocrinology 107:1291–1299; 1980.

20. Tamai, N.; Myoui, A.; Tomita, T.; Nakase, T.; Tanaka, J.; Ochi, T.; Yoshikawa, H. Novel hydroxyapatite ceramics with an interconnective porous structure exhibit superior osteoconduction in vivo. J. Biomed. Mater. Res. 59:110–117; 2002.

21. Uchida, A.; Araki, N.; Shinto, Y.; Yoshikawa, H.; Kurisaki, H.; Ono, K. The use of calcium hydroxyapatite ceramic in bone tumor surgery. J. Bone Joint Surg. Br. 72:298–302; 1990.

22. van Blitterswijk, C. A.; Hesseling, S. C.; Grote, J. J.; Koerten, H. K.; deGroot, K. The biocompatibility of hydroxyapatite ceramics: A study of retrieved human middle ear implants. J. Biomed. Mater. Res. 24:433–453; 1990.

23. Whang, K.; Thomas, C. H.; Healy, K. E.; Nuber, G. A novel method to fabricate bioabsorbable scaffolds. Polymer 36:837–842; 1995.

24. Yoshikawa, T.; Ohgushi, H.; Okumura, M.; Tamai, S.; Dohi, Y.; Moriyama, T. Biochemical and histological sequences of membranous ossification in ectopic site. Calcif. Tissue Int. 50:184–188; 1992.

25. Yoshikawa, T.; Ohgushi, H.; Tamai, S. Immediate bone forming capability of prefabricated osteogenic hydroxyapatite. J. Biomed. Mater. Res. 32:481–492; 1996.

Effects of rotation on measurement of lower limb alignment for knee osteotomy
Hideo Kawakami; Nobuhiko Sugano; Kazuo Yonenobu; Hideki Yoshikawa; et al
Journal of Orthopaedic Research; Nov 2004; 22, 6; ProQuest Medical Library
pg. 1248

Effects of rotation on measurement of lower limb alignment for knee osteotomy

Hideo Kawakami [a,*], Nobuhiko Sugano [b], Kazuo Yonenobu [c],
Hideki Yoshikawa [b], Takahiro Ochi [a], Asaki Hattori [d], Naoki Suzuki [d]

[a] *Department of Medical Robotics and Image Sciences, Division of Robotic Therapy, Osaka University Graduate School of Medicine,
2-2 Yamadaoka, Suita, Osaka 565-0871, Japan*
[b] *Department of Orthopaedic Surgery, Osaka University Graduate School of Medicine, 2-2 Yamadaoka, Suita, Osaka 565-0871, Japan*
[c] *Department of Orthopaedic Surgery, Osaka-Minami National Hospital, Osaka 586-0008, Japan*
[d] *Institute for High Dimensional Medical Imaging, Jikei University School of Medicine, Komae, Tokyo 201-8601, Japan*

Abstract

The purposes of this study were to clarify the effects of rotation on two-dimensional measurement of lower limb alignment for knee osteotomy using a three-dimensional method and to determine whether this 3-D simulation method could help with planning of knee osteotomy. We developed computer software to calculate femorotibial angle (FTA) and hip–knee–ankle angle (HKA) and simulate knee osteotomy from a CT-based 3-D bone model of the lower limb. Lower limb rotation on anteroposterior long-standing radiographs was measured by superimposing the 3-D bone models. Changes in alignment with limb rotation were calculated using the software. FTA after virtual closed-wedged osteotomy was measured for a hypothetical case of a rotation error of the osteotomy plane in reattaching the proximal cutting surface to the distal cutting surface. For 31 varus knees in 20 patients with medial compartment arthritis, the mean rotation angle, relative to the epicondylar axis, with variable limb position was $7.4 \pm 3.9°$ of internal rotation (mean $\pm$ SD), ranging from 8° of external rotation to 14° of internal rotation; the mean changes in FTA and HKA were $3.5 \pm 2.2°$ (range, 0.4–8.6) and $1.6 \pm 1.3°$ (range, 0.2–4.9), respectively. The FTA "flexion angle" (lateral view alignment from neutral AP) and the absolute HKA "flexion angle" correlated with the change in FTA and HKA with limb rotation, respectively (FTA, $R = 0.999$; HKA, $R = 0.993$). The mean change in FTA after virtual closed-wedged osteotomy was 3.2° for internal and external 10° rotation errors in reattaching the osteotomy plane. Rotation may affect measurement of lower limb alignment for knee osteotomy, and 3-D methods are preferable for surgical planning.
© 2004 Orthopaedic Research Society. Published by Elsevier Ltd. All rights reserved.

Keywords: Lower limb alignment; High tibial osteotomy; 3-D CT simulation

Introduction

High tibial osteotomy (HTO) is a treatment option for medial compartment osteoarthritis (OA) of the knee. The goal of HTO is to reduce abnormal loads. The expected survival rate is approximately 85% at 5 years and 60% at 10 years [5,7,9,10,18,19,23]. Factors that affect outcome include operative factors [5,17,23] and patient factors, including pre-operative grade of OA, age, obesity, and range of motion [3,9]. Measurement of lower limb alignment on plain radiographs is used as an

alternative indicator of the loading imbalance because of difficulties in measuring the load on the medial and lateral surfaces of the knee joint non-invasively.

Correction of lower limb alignment is one of the most critical operative factors; appropriate correction yields good to excellent results (success rate of 87–100% at 5–10 years), but inappropriate correction (under- or over-correction) yields poor results (success rate of 26–63% at 5–10 years) [5,7,19]. The recommended alignment varies widely, with recommended hip–knee–ankle angles (HKA) ranging from 2° to 7° [5,7,10,13] and femorotibial angles (FTA) ranging from 164° to 175° [9,12,15,21,23]. Conventionally, pre-operative lower limb alignment has been measured two-dimensionally on AP long-standing radiographs of the lower limb, but variability of rotation in positioning of the limb during radiography can affect

---
* Corresponding author. Tel.: +81-6-6879-3552; fax: +81-6-6879-3869.
E-mail address: hkawakami-osk@umin.ac.jp (H. Kawakami).

measurements. The effects of rotation on lower limb alignment have been reported [14,20,22], but based only on theoretical assessments.

Intra-operative osteotomy plane rotation cannot be simulated using two-dimensional radiographs. Thus, pre-operative planning based on AP radiographs and an intra-operative technique with osteotomy plane rotation could cause inappropriate correction of lower limb alignment. To clarify the effects of rotation on knee osteotomy and to facilitate pre-operative planning using 3-D images, we developed computer software that measures lower limb alignment in 3-D images and simulates knee osteotomy. In the present study, we examined 31 knees in twenty patients with medial compartment OA in varus knees to clarify important issues regarding alignment and planning.

Materials and methods

The patients were 7 men and 13 women ranging in age from 31 to 85 years (mean, 64.8 years). Using the Kellgren and Lawrence radiographic classification of OA [11], 11 knees (36%) had grade 2, indicating osteophytes and possible joint space narrowing, 15 knees (48%) had grade 3, indicating moderate multiple osteophytes, definite joint space narrowing, some sclerosis, and possible bone contour deformity, and 5 knees (16%) had grade 4, indicating large osteophytes, marked joint space narrowing, severe sclerosis, and definite bone contour deformity. There were no severe degenerative changes in the patellofemoral or lateral femorotibial articulations. The average Knee Society score [8] was 53 ± 22 points, and the average functional score was 73 ± 21 points. All patients were completely informed about this study and consented to the examination.

AP long-standing radiographs of the lower limb were taken while the radiologist carefully attempted to position the patella facing forward. Transverse images from the proximal end of the femur to the distal end of the tibia were obtained using a helical CT scanner. To match the position during stance, the positioning during the scan was with the knee in full extension and the ankle joint at 90° of flexion, with an ankle braced in the supine position. Slice thickness and slice pitch were: 3 mm for the femoral head; 10 mm for the femoral shaft; 2 mm for the segment from 10 mm above the femoral epicondyles to the top of the tibial eminence; 1 mm for the segment from the tibial eminence to 10 mm below the tibial eminence; 2 mm for the segment from 10 mm below the tibial eminence to the tibial tuberosity; 10 mm for the tibial shaft; and 2 mm for the segment from 10 mm above the ankle joint to 10 mm below the ankle joint.

We reconstructed 3-D skeletal models of the femur, tibia, and patella from the CT images, using surface rendering software (Analyze PC 3.0, Mayo Foundation, Rochester, MN). To define the knee joint coordinates, 4 landmark points were plotted on the 3-D surface models. The first point (F) was the center of the femoral head, which was designated as the center of the best-fit sphere. The second and third points (LE and ME) were the top of the medial and lateral femoral epicondyles, respectively. The fourth point (TD) was the centroid of multiple points on the distal tibial joint surface that were surrounded by a manually drawn circle. Based on these points, the coordinates of the knee joint were defined to indicate the front of the knee (neutral position) and the axis of the lower limb rotation (Fig. 1). The vertical Z-axis was defined as the line through F and TD. This line is sometimes referred to as the initial mechanical axis of the lower extremity. A transverse plane, TP, was defined as the plane perpendicular to Z (the mechanical axis of the lower extremity) and passing through the medial epicondyle; i.e., including the point ME. The point LEp was defined as the projection of the lateral epicondyle (LE) onto this transverse plane. LEp was projected along a line parallel to Z, extending from LE to the transverse plane TP. The X-axis, representing a neutral medial to lateral direction, was defined as the axis
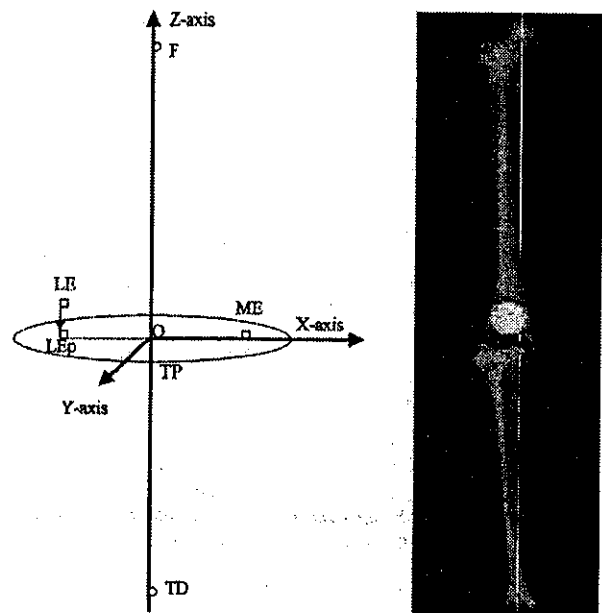

Fig. 1. The coordinates defining the front of the knee. Z-axis, the axis of lower limb rotation; F, the center of the femoral head; ME, the medial epicondyle; LE, the lateral epicondyle; TD, the center of gravity of the distal tibia joint surface.

containing the line ME-LEp; i.e., the epicondylar projection. The X-axis was perpendicular to Z, contained the transverse plane, was parallel to ME-LEp, and (being an axis) defined the origin of Z. The Y-axis passed through the intersection of axes X and Z and was perpendicular to each. The Y-axis was therefore a neutral AP axis of the distal femur, and for our purposes, was the neutral AP vector for the knee itself. The front of the knee was defined from the transepicondylar axis, because the transepicondylar axis is a reliable rotational landmark not affected by distortion of the femoral condyles [2].

To measure lower limb axial alignment from 3-D images, we developed computer software that projected the 3-D models on a two-dimensional XZ plane (the plane of the mechanical axis Z and the projected epicondylar axis EM-ELp) and calculated the angle. FTA and HKA were used as indices of lower limb alignment [1,16]. FTA is the lateral angle at the intersection between the femoral shaft axis and the tibial shaft axis, and HKA is the medial angle deviation from 180° at the intersection between the mechanical axes of the femur and tibia, plus for valgus alignment and minus for varus alignment.

To measure FTA from 3-D images, the femoral shaft axis was defined as the line through the centroid of multiple points on the femoral transverse sections at 25% of the femoral length below the center of the femoral head and at 20% of the femoral length above the point M on the epicondylar axis EM-ELp. The point M was the intersection of the epicondylar axis EM-ELp and the line perpendicular to EM-ELp that passes through the center of the femoral head. The femoral length was defined as the distance from the center of the femoral head to the point M. The tibial shaft axis was defined as the line through the centroid of multiple points on the tibial transverse sections at 20% of the tibial length below the proximal end of the tibia and at 20% of the tibial length above the distal end of the tibia. The tibial length was defined as the distance from the midpoint between the tips of the medial and lateral tibial spines and the centroid of the multiple points on the distal tibia joint surface.

To measure HKA from 3-D images, the mechanical axis of the femur was defined as the line through the center of the femoral head and the midpoint between the tips of the medial and lateral tibial spines, and the mechanical axis of the tibia was defined as the line through the midpoint between the tips of the medial and lateral tibial spines and the centroid of the multiple points on the distal tibia joint surface.

To study the variable positioning of the limb by the radiologist, the lower limb rotation on the AP long-standing radiographs was measured by superimposing the 3-D bone models on the radiograph, taking into account the relative position of the patellar and femoral outlines obtained from the radiographs. Next, the 3-D model was rotated around the Z-axis in the computer simulation. The relative positions of the patella and femur in the models were superimposed on the patellar and femoral outlines from the radiograph. The relative positions of the patella and femur in the models were matched to the patellar and femoral outlines of the radiograph by rotating the models in the computer simulation. We also measured the rotation angle of the models from the neutral position (the Y-axis in the knee coordinate system).

The 3-D bone model was rotated from the neutral position to the maximum rotation obtained from radiographic measurements for all patients. Based on limb rotation in the computer simulation, possible changes in FTA and HKA with limb rotation were calculated using the computer software.

To study correlations between apparent axial deformity of the lower limb and variation in FTA and HKA with limb rotation, we measured and analyzed FTA and HKA on AP long-standing radiographs of the lower limb, the "flexion angle" of FTA and HKA calculated by the computer software, and the change in FTA and HKA with limb rotation. The "flexion angle" was defined as the angle from a lateral view of those axes, specifically normal to the neutral AP, viewed along the line of the ML rotational axis of the femur. The "flexion angles" of FTA and HKA were calculated with lateral projections of FTA and HKA using the computer software. The changes in FTA and HKA were calculated by the reduction of the minimum angle from the maximum angle in the range of rotation from radiographic measurements. Polynomial regression models were used to check the relationships between the axis deformity of the lower limb and the changes in FTA and HKA with limb rotation.

We developed computer software that simulates knee osteotomy by cutting the bone models in any plane, removing the wedged bone, and reattaching or opening the surfaces in the coordinate of the tibia. The coordinate of the tibia was defined as follows. The points Mt and Lt on medial and lateral joint surfaces of the proximal tibia were defined as the centroid of multiple points on the joint surface that were surrounded by a manually drawn circle. The line through the points Mt and Lt was defined as the joint line of the proximal tibia joint surface. The Zt-axis, representing the vertical, was defined as the line through TD and the mid-point of MT and LT. The transverse plane TPt was defined as the plane perpendicular to the Zt-axis and passing through the point Mt. The Xt-axis was the line through the point Mt and the intersection of the Zt-axis and the transverse plane TPt. The Yt-axis was perpendicular to the Zt- and Xt-axis.

Using this computer software, we simulated knee osteotomy to help with pre-operative planning on the computer display. To examine the effect of intra-operative osteotomy plane rotation on changes in axial alignment, we simulated closed-wedge HTO. The osteotomy plane was parallel to the tibial articular surface at 25 mm below the joint line through the point Mt and the point Lt. The target post-operative alignment was set at 4° of HKA. Rotation error of the osteotomy plane may affect determination of the direction of the cutting plane and reattachment of the cutting surfaces. FTA and HKA after virtual knee osteotomy were measured for a hypothetical case of internal and external 15° osteotomy plane rotation in the cutting plane direction of the proximal tibia. This osteotomy plane was twisted around the Zt-axis. FTA and HKA after virtual knee osteotomy were measured for a hypothetical case of internal and external 15° osteotomy plane rotation in reattaching the proximal cutting surface to the distal cutting surface. This osteotomy plane was twisted around the shaft parallel to the Zt-axis through the point of the medial wedge on the osteotomy plane (Fig. 2).

Results

The mean FTA and HKA on AP long-standing radiographs of the lower limb was 183.5 ± 5.5° (mean ± SD; range, 178–205) and −9.2 ± 5.6° (range, −30 to −4),
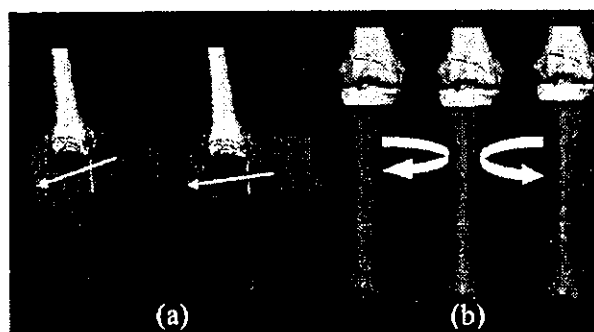

Fig. 2. Operative simulation of HTO: (a) osteotomy plane rotation in the cutting plane direction of the proximal tibia. (b) Osteotomy plane rotation in reattaching the proximal cutting surface to the distal cutting surface.

respectively. The mean rotation angle with variable limb position was 7.4 ± 3.9° of internal rotation, ranging from 8° of external rotation to 14° of internal rotation from the neutral position (the Y-axis in the coordinate system of the knee). Within the range of rotation angles, we calculated the difference between the minimum axial alignment angle and the maximum axial alignment angle. The mean change in FTA with limb rotation was 3.5 ± 2.2° (range, 0.4–8.6), and the mean change in HKA was 1.6 ± 1.3° (range, 0.2–4.9).

The change in FTA with limb rotation increased as the "flexion angle" of FTA increased (Table 1 and Fig. 3a). The change in HKA with limb rotation increased as the absolute "flexion angle" of HKA increased (Fig. 3b). A positive correlation was found between the "flexion angle" of FTA (FFTA) and the change in FTA with lower limb rotation (CFTA), with a straight regression line (CFTA = 0.386, FFTA−2.696) and a correlation coefficient of 0.999 (Fig. 3c). A positive correlation existed between the absolute "flexion angle" of HKA (AFHKA) and the change in HKA with lower limb rotation (CHKA), with a straight regression line (CHKA = 0.381, AFHKA+0.009) and a correlation coefficient of 0.993 (Fig. 3d). No significant correlation was found between alignment on AP radiographs and the change in alignment with lower limb rotation ($R = 0.357$ for FTA; $R = 0.319$ for HKA).

For the hypothetical case of internal and external 5°, 10° and 15° osteotomy plane rotation, the change in FTA was 0.2 ± 0.1°, 0.4 ± 0.3° and 0.8 ± 0.4°, respectively, and the change in HKA was 0.2 ± 0.1°, 0.4 ± 0.2° and 0.7 ± 0.3°, respectively. Closed-wedged osteotomy was also simulated for a hypothetical case of osteotomy plane rotation in reattaching the proximal cutting surface to the distal cutting surface. For the hypothetical case of internal and external 5°, 10° and 15° osteotomy plane rotation, the change in FTA was 1.6 ± 0.6°, 3.2 ± 1.1° and 4.8 ± 1.7°, respectively, and the change in HKA was 0.9 ± 0.5°, 1.9 ± 1.0° and 2.8 ± 1.5°, respectively.

Table 1
FTA and HKA on AP radiographs, the "Flexion angle" of FTA and HKA calculated using the computer software, and the change in FTA and HKA with lower limb rotation (31 varus knees of 20 patients)

Knee number	Gender[a]	FTA on AP radiograph	"Flexion angle" of FTA[b]	Change in FTA with limb rotation[c]	HKA on AP radiograph	"Flexion angle" of HKA[b]	Change in HKA with limb rotation[c]
1	F	178.0	2.6	0.9	−5.0	5.9	2.2
2	F	178.0	5.9	2.2	−4.0	2.6	0.9
3	F	178.0	7.2	2.7	−4.0	1.8	0.6
4	F	179.0	6.3	2.4	−4.0	2.9	1.0
5	F	179.0	5.4	2.0	−5.0	4.7	1.8
6	M	179.0	15.9	6.1	−4.0	−6.7	2.6
7	M	180.0	2.5	0.9	−8.0	6.3	2.3
8	F	180.0	11.6	4.4	−6.0	−2.2	0.9
9	M	181.0	7.6	2.9	−7.0	1.2	0.3
10	M	181.0	17.5	6.8	−7.0	−7.4	3.0
11	M	181.0	10.4	4.1	−7.0	−1.9	0.9
12	M	181.0	12.3	4.7	−8.0	−2.2	1.0
13	F	181.0	8.8	3.4	−8.0	1.9	0.6
14	F	182.0	10.2	4.0	−7.0	−0.6	0.4
15	M	182.0	8.5	3.3	−9.0	2.8	0.9
16	M	182.0	3.0	1.1	−9.0	7.3	2.7
17	M	182.0	7.4	2.8	−5.0	−0.3	0.2
18	M	182.0	20.8	8.0	−6.0	−11.4	4.5
19	F	182.0	22.4	8.6	−7.0	−12.6	4.9
20	F	183.0	3.4	1.3	−11.0	3.9	1.3
21	F	183.0	10.7	4.0	−5.0	−0.3	0.2
22	F	185.0	10.7	4.1	−11.0	−1.8	0.8
23	F	185.0	12.1	4.6	−11.0	−4.8	1.9
24	M	186.0	3.9	1.6	−10.0	6.7	2.3
25	F	186.0	6.0	2.4	−15.0	2.4	0.7
26	F	187.0	0.7	0.4	−11.0	7.9	2.8
27	F	187.0	3.3	1.4	−11.0	4.8	1.6
28	F	188.0	7.4	2.9	−14.0	−0.6	0.4
29	F	188.0	5.9	2.3	−12.0	0.8	0.2
30	F	196.0	9.7	3.9	−23.0	−0.2	0.6
31	F	205.0	20.4	8.0	−30.0	−10.9	4.5

[a] F: female, M: male.
[b] "Flexion angle" was defined as the angle from a lateral view of AP neutral position.
[c] Change in limb alignment was calculated by the reduction of the minimum angle from the maximum angle within the range of rotation from the neutral position.

Discussion

In a study of the effect of rotation on lower limb axial alignment, Wright et al. [22] found that limb rotation of 10° internally and externally had only a small effect on FTA in radiographs of amputated lower extremities. Swanson et al. [20] reported that limb rotation of 10° internally and externally had a statistically significant effect on FTA in radiographs of Sawbone extremity models with severe valgus or varus deformity. Krackow et al. [14] analyzed the effect of flexion and rotation on varus and valgus deformity by calculating the assumed leg deformity. With rotation and flexion of up to 10° each, the artifactual contributions to axial deformity were very small at less than 2° of HKA, but with flexion and rotation of 10–20° each, the changes became significant at up to 7.4° of HKA.

These previous studies did not include clinical patients and were only theoretical assessments. The present

study involved 31 varus knees of patients with medial compartment OA. Radiographic measurements were obtained under clinical conditions, and the mean change in FTA and HKA within the range of rotation was 3.5° (range, 0.4–8.6) and 1.6° (range, 0.2–4.9), respectively. The present results show a measurement error that may occur in assessment of lower limb alignment in clinical situations. When measuring lower limb alignment and planning knee osteotomy on radiographs, the extent of variation of lower limb alignment with limb rotation should be considered.

In previous studies, it was unclear what factors were involved in changes in lower limb alignment with limb rotation. In the present study, we examined the "flexion angle" of FTA and the "flexion angle" of HKA. The "flexion angle" was defined as the angle from a lateral view of those axes and was considered to be the flexion angle of the knee during radiography. The "flexion angle" of FTA and the absolute "flexion angle" of HKA
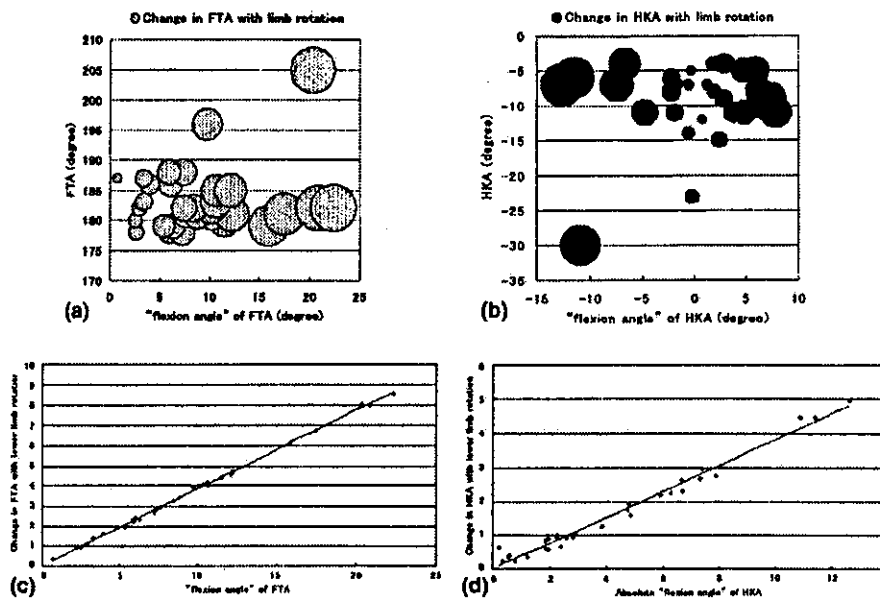
Fig. 3. Relationship between FTA and HKA on AP radiograph, the "flexion angle" of FTA and HKA calculated using the computer software, and the change in FTA and HKA with limb rotation. (a) The change in FTA increased as the "flexion angle" of FTA increased. (b) The change in HKA increased as the absolute "flexion angle" of HKA increased. (c) The linear regression line between the "flexion angle" of FTA and the change in FTA with lower limb rotation. (d) The linear regression line between the absolute "flexion angle" of HKA and the change in HKA with lower limb rotation.

were highly correlated with changes in FTA and HKA with limb rotation, respectively. However, no significant correlation was found between alignment on AP radiographs and the change in alignment with lower limb rotation. Thus, our findings show that the "flexion angle" of the knee during radiography was the main source of the effect of rotation on limb alignment, rather than the varus deformity of the knee on clinical radiographs.

In the present study, the effect of rotation on limb alignment increased as the "flexion angle" increased. The "flexion angle" of FTA tended to be larger than the absolute "flexion angle" of HKA because the center of the femoral head (including the line of HKA) is always anterior to the femoral shaft axis in anteversion of the femoral head and because the midpoint between the tibial spines (including the line of HKA) is often posterior to femoral shaft axis. The mean change in FTA with limb rotation was greater than the mean change in HKA with limb rotation. Thus, HKA should be used for assessment of lower limb alignment on radiographs when the "flexion angle" of the lower limb alignment is large.

Previously, two groups reported on computer-assisted knee osteotomy. Chao et al. developed a 2-D rigid-body spring model to simulate the forces across the articular surfaces [4]. Ellis et al. used a 3-D pre-surgical planner and an intra-operative guidance system [6]. The 3-D pre-surgical planner provides a 3-D model, but only around the knee joint. We developed computer software that simulates knee osteotomy and calculates axial alignment over the full length of the lower extremities.

The present 3-D system allowed us to precisely analyze pre- and post-operative lower limb alignment. We were able to simulate the changes in FTA and HKA with limb rotation and intra-operative osteotomy plane rotation. This system proved useful for pre-operative planning of knee osteotomy.

No clinical reports exist concerning the effect of osteotomy plane rotation on axial alignment in knee osteotomy. The present study simulated the effect of osteotomy plane rotation on lower limb alignment for the direction of the osteotomy plane and reattachment of the osteotomy plane within internal and external rotation of 15°. The rotation in reattachment of the osteotomy plane affected lower limb alignment, whereas the rotation in the direction of the osteotomy plane did not. In the case of internal and external 10° rotations in reattaching the proximal cutting surface to the distal cutting surface, the mean changes in FTA and HKA were 3.2° and 1.9°, respectively. Thus, intra-operative technique with rotation factor can affect lower limb alignment after knee osteotomy. The present 3-D method is useful for precise assessment of lower limb alignment after knee osteotomy.

Bony landmarks for determining the 3-D coordinate of the lower limb are not easily identified or repeatable. In the present system, we obtained thin-slice CT images around the landmark points to facilitate identification. To examine measurement accuracy of lower limb alignment using this 3-D method, one orthopaedic surgeon plotted the six landmarks, and five trials were performed

Table 2
Measurement errors of this system by plotting bone land marks

Trial	Subject 1		Subject 2		Subject 3		Subject 4		Subject 5	
	FTA	HKA	FTA	HKA	FTA	HKA	FTA	HKA	FTA	HKA
1	178.9	−5.0	179.7	−6.7	184.2	−10.2	185.6	−10.4	184.1	−7.1
2	179.0	−5.1	179.9	−6.8	184.0	−10.4	185.5	−10.5	184.0	−7.1
3	178.9	−5.0	179.9	−6.7	184.0	−10.2	185.5	−10.4	184.2	−6.9
4	178.9	−5.1	179.7	−6.6	184.1	−10.4	185.4	−10.6	184.3	−7.1
5	178.9	−4.9	179.7	−6.7	184.0	−10.4	185.7	−10.5	184.1	−7.2
Error range	0.1	0.2	0.2	0.2	0.3	0.3	0.3	0.3	0.3	0.2

with five subjects. The error range was within 0.3° for both HKA and FTA (Table 2). This appears to be acceptable for assessment of lower limb alignment.

A limitation of this study was comparability of CT scans taken in a supine position to radiographs taken in a weight-bearing position. Generally, lower limb alignment is measured using AP long-standing radiographs. Although we did not obtain CT images in the standing position, we used CT images in a semi-standing position, taken with the knee in full extension and the ankle joint at 90° of flexion with an ankle brace in the supine position.

Acknowledgements

References

[1] Bauer GC, Insall J, Koshino T. Tibial osteotomy in gonarthrosis. J Bone Joint Surg Am 1969;51(8):1545–63.

[2] Berger RA, Rubash HE, Seel MJ, et al. Determining the rotational alignment of the femoral component in total knee arthroplasty using the epicondylar axis. Clin Orthop 1993; 286(January):40–7.

[3] Berman AT, Bosacco SJ, Kirshner S, et al. Factors influencing long-term results in high tibial osteotomy. Clin Orthop 1991; 272(November):192–8.

[4] Chao EY, Sim FH. Computer-aided preoperative planning in knee osteotomy. Iowa Orthop J 1995;15:4–18.

[5] Coventry MB, Ilstrup DM, Wallrichs SL. Proximal tibial osteotomy. A critical long-term study of eighty-seven cases. J Bone Joint Surg Am 1993;75(2):196–201.

[6] Ellis RE, Tso CY, Rudan JF, Harrison MM. A surgical planning and guidance system for high tibial osteotomy. Comput Aided Surg 1999;4(5):264–74.

[7] Hernigou P, Medevielle D, Debeyre J, Goutallier D. Proximal tibial osteotomy for osteoarthritis with varus deformity. A ten to thirteen-year follow-up study. J Bone Joint Surg Am 1987;69(3): 332–54.

[8] Insall JN, Dorr LD, Scott RD, et al. Rationale of the Knee Society clinical rating system. Clin Orthop 1989;248(November):13–4.

[9] Insall JN, Joseph DM, Msika C. High tibial osteotomy for varus gonarthrosis. A long-term follow-up study. J Bone Joint Surg Am 1984;66(7):1040–8.

[10] Ivarsson I, Myrnerts R, Gillquist J. High tibial osteotomy for medial osteoarthritis of the knee. A 5 to 7 and 11 year follow-up. J Bone Joint Surg Br 1990;72(2):238–44.

[11] Kellgren JH, Lawrence JS. Radiological assessment of osteoarthrosis. Ann Rheum Dis 1957;6:494–502.

[12] Kettelkamp DB, Wenger DR, Chao EY, Thompson C. Results of proximal tibial osteotomy. J Bone Joint Surg Am 1976;58(7):952–60.

[13] Krackow KA, Matthew JP. High tibial osteotomy and distal femoral osteotomy for valgus or varus deformity around the knee. AAOS Instructional Course Lecture, vol. 47, 1998. p. 429–36.

[14] Krackow KA, Pepe CL, Galloway EJ. A mathematical analysis of the effect of flexion and rotation on apparent varus/valgus alignment at the knee. Orthopedics 1990;13(8):861–8.

[15] MacIntosh DL, Welsh RP. Joint debridement—a complement to high tibial osteotomy in the treatment of degenerative arthritis of the knee. J Bone Joint Surg Am 1977;59(8):1094–7.

[16] Moreland JR, Bassett LW, Hanker GJ. Radiographic analysis of the axial alignment of the lower extremity. J Bone Joint Surg Am 1987;69(5):745–9.

[17] Rinonapoli E, Mancini GB, Corvaglia A, Musiello S. Tibial osteotomy for varus gonarthrosis. A 10- to 21-year followup study. Clin Orthop 1998;353(Aug):185–93.

[18] Ritter MA, Fechtman RA. Proximal tibial osteotomy. A survivorship analysis. J Arthroplasty 1988;3(4):309–11.

[19] Rudan JF, Simurda MA. Valgus high tibial osteotomy. A long-term follow-up study. Clin Orthop 1991;268(July):157–60.

[20] Swanson KE, Stocks GW, Warren PD, et al. Does axial limb rotation affect the alignment measurements in deformed limbs? Clin Orthop 2000;371(February):246–52.

[21] Vainionpaa S, Laike E, Kirves P, Tiusanen P. Tibial osteotomy for osteoarthritis of the knee. A five to ten-year follow-up study. J Bone Joint Surg Am 1981;63(6):938–46.

[22] Wright JG, Treble N, Feinstein AR. Measurement of lower limb alignment using long radiographs. J Bone Joint Surg Br 1991; 73(5):721–3.

[23] Yasuda K, Majima T, Tsuchida T, Kaneda K. A ten- to 15-year follow-up observation of high tibial osteotomy in medial compartment osteoarthrosis. Clin Orthop 1992;282(September):186–95.

2399

LOW-INTENSITY PULSED ULTRASOUND ACCELERATES MATURATION OF CALLUS IN PATIENTS TREATED WITH OPENING-WEDGE HIGH TIBIAL OSTEOTOMY BY HEMICALLOTASIS

BY NORIYUKI TSUMAKI, MD, MASAAKI KAKIUCHI, MD, JIRO SASAKI, TAKAHIRO OCHI, MD, AND HIDEKI YOSHIKAWA, MD

Investigation performed at the Department of Orthopaedics, Osaka University Graduate School of Medicine, and the Department of Orthopaedic Surgery and Radiology, Osaka Police Hospital, Osaka, Japan

Background: Opening-wedge high tibial osteotomy by hemicallotasis for osteoarthritis in the medial compartment of the knee requires external fixation for a long time, until callus maturation is complete. The aim of this study was to determine if low-intensity pulsed ultrasound would accelerate callus maturation when applied after distraction to limbs treated with opening-wedge high tibial osteotomy by hemicallotasis.

Methods: Twenty-one patients with symmetric grades of osteoarthritis and similar degrees of varus deformity in the two knees underwent bilateral one-stage opening-wedge high tibial osteotomy by hemicallotasis. After completion of distraction, the bone mineral density of the distraction callus was measured. Then, one randomly selected limb was subjected to ultrasound treatment for twenty minutes daily until removal of the external fixator. The contralateral limb was left untreated to serve as the control. After four weeks of treatment, bone mineral density was measured again.

Results: During the four-week treatment period, the mean increase in callus bone mineral density was significantly greater in the ultrasound-treated tibiae (0.20 ± 0.12 g/cm^2) than in the control tibiae (0.13 ± 0.10 g/cm^2) ($p = 0.02$, unpaired t test). In eighteen patients the increase in the bone mineral density was greater in the ultrasound-treated limb than in the control limb, whereas in three patients the increase was greater in the control limb.

Conclusions: We found that low-intensity pulsed ultrasound applied during the consolidation phase of distraction osteogenesis accelerates callus maturation after opening-wedge high tibial osteotomy by hemicallotasis in elderly patients.

Level of Evidence: Therapeutic study, Level I-1a (randomized controlled trial [significant difference]). See Instructions to Authors for a complete description of levels of evidence.

Ultrasound, a form of mechanical energy that produces micromechanical strain when transmitted through the body, is widely used in medicine as a therapeutic and diagnostic tool. In vitro studies have demonstrated that low-intensity pulsed ultrasound alters metabolism at the cellular level. Micromechanical strain caused by ultrasound transmission through the body can promote bone formation in a manner comparable with the bone responses to mechanical stress postulated by Wolff's law[1,2]. Studies of animals have demonstrated that low-intensity pulsed ultrasound increases the rate of endochondral bone formation and the structural strength of fracture sites[3,4]. Clinical investigations have shown that low-intensity pulsed ultrasound improves healing of pseudarthroses, delayed unions, and nonunions[5]. Randomized, double-blind, controlled clinical trials have shown that the technique accelerates the repair process in fractures of the tibia[6] and radius[6]. These studies have established the clinical usefulness of low-intensity pulsed ultrasound for acceleration of fracture-healing[5].

Callotasis and hemicallotasis are useful techniques to correct limb deformity or to lengthen the limb[7], but the distraction callus heals very slowly, requiring patients to wear an

external fixator for a long period. The effects of low-intensity pulsed ultrasound on healing of the distraction callus have been examined in animal models[9,10] but have not been assessed in a clinical setting, to our knowledge.

Opening-wedge high tibial osteotomy by hemicallotasis, a surgical intervention for patients with osteoarthritis in the medial compartment of the knee, has the advantage of accurate correction[11]. However, the technique requires external fixation until the distraction callus is mature, and a high rate of pin-site infection has been reported[16].

In this randomized study, we quantitatively examined the effects of low-intensity pulsed ultrasound on the maturation of the distraction callus during the consolidation phase in patients treated with an opening-wedge high tibial osteotomy by hemicallotasis.

Materials and Methods
Patient Selection

From 1999 to 2002, bilateral one-stage opening-wedge high tibial osteotomy by hemicallotasis was performed in thirty-three patients who had bilateral osteoarthritis in the medial compartment of the knee with bilateral knee pain. Selection criteria for the present study included (1) bilaterally symmetric grades of osteoarthritis according to the classification of Kellgren and Lawrence[17], and (2) a difference of ≤3° in varus deformity between the left and right sides as indicated by the femorotibial angles measured on full-length radiographs of the lower limbs with the patient standing. Twenty-one patients (seventeen women and four men) who met these criteria consented to participate in the study. The ages of the patients ranged from fifty-three to seventy-eight years (average, sixty-eight years). The severity of the medial osteoarthritis was grade 2 in four knees, grade 3 in thirty knees, and grade 4 in eight knees. The study was approved by our hospital review board.

Operative Technique

Opening-wedge high tibial osteotomy was performed with use of an articulated dynamic axial fixator with a proximal T-clamp (hemicallotasis device; Orthofix 20-010 and CP-0029; Orthofix, Bussolengo, Italy). During the surgery, four tapered half-pins (Orthofix; 6 mm/5 mm) were inserted; two with cancellous threads were placed at the proximal sites and two with cortical threads, at the distal sites. For the osteotomy, an anteromedial approach was used, with a transverse incision of the skin and a longitudinal incision of the periosteum followed by elevation. The position and direction of the osteotomy were monitored in both the coronal and the sagittal plane with use of radiography during the operation. Osteotomy of the medial three-quarters of the proximal part of the tibia was carried out just proximal to the tibial tubercle. We used an osteotome to cut the anterior and middle portions of the tibia, and we used an oscillating saw to cut the posterior cortex. The status of the cortex lateral to the osteotomy site was assessed by testing the rigidity of the osteotomy site with manual valgus stress. The Orthofix fixator was applied, and distraction was performed for 5 mm to ensure that the intact portion lateral to the osteotomy site acted as a hinge. Then the fixator was compressed so that there was good osseous apposition. The periosteum was closed. A fibular osteotomy was not performed. As with callus distraction for limb-lengthening, the osteotomy was followed by periods of latency, distraction, and consolidation until removal of the external fixator. Patients were allowed full weight-bearing throughout these periods.

Distraction and Consolidation

After a latency period of fourteen days, distraction was begun. Radiographs of the osteotomy sites in both limbs were made once a week throughout the distraction and consolidation phases. Additional radiographs were made according to the symptoms and findings of previous radiographs. The compression/distraction unit was elongated at a rate of 1 mm daily, with two 0.5-mm distractions each day. Distraction was stopped and the consolidation phase was begun when the hip-ankle mechanical axis of the limb passed the medial one-ninth to one-third of the lateral compartment of the tibial plateau as seen on a full-length radiograph of the limb with the patient standing. The locking bolt of the telescopic body of the fixator was then tightened.

The consolidation period was ended when the callus was considered strong enough for safe removal of the fixator without the risk of fracture (i.e., when there was a smooth uninterrupted cortical margin medial to the regenerated bone or an uninterrupted trabecular pattern occupying the lateral two-thirds of the tibia on an anteroposterior radiograph). The assessors of callus consolidation were not blinded to the use of low-intensity pulsed ultrasound. A few days after release of the locking screw (at a mean [and standard deviation] of 1.5 ± 0.6 days; range, one to three days), the fixator was removed and the pins were left in place for a trial period of several more days. The pins were removed after radiographs confirmed that there was no evidence of collapse of the callus.

Measurement of Bone Mineral Density

Although we performed the osteotomy perpendicular to the long axis of the lower limb in the sagittal plane, the postoperative anteroposterior radiograph of the proximal part of the tibia revealed that the osteotomy was not perfectly parallel to the x-ray beam in some patients. Before measuring bone mineral density, all patients were placed in the supine position with the knees in neutral rotation under the x-ray tube. The knee joint was slightly flexed (Fig. 1-A) or the entire limb was raised (Fig. 1-B), so that the beam would pass parallel to the osteotomy. As a result, we obtained an anteroposterior view of the callus without an overlap of the anterior or posterior cortical bone of the tibia. We carefully recorded the position of each limb of each patient by measuring the distance and angle of the fixators relative to the bed on which the patient lay. To measure the bone mineral density of the distraction callus, the patient was then placed on a dual-energy x-ray absorptiometry unit (QDR-2000; Hologic, Boston, Massachusetts) with the limb in the same position as determined under the x-ray
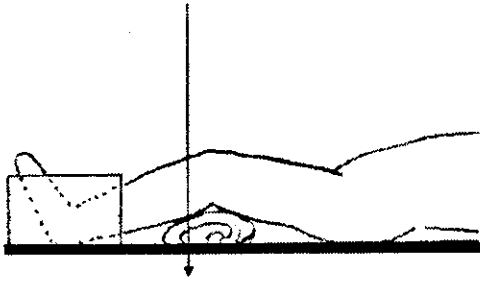
LOW-INTENSITY ULTRASOUND ACCELERATES CALLUS
MATURATION IN TIBIAL OSTEOTOMY BY HEMICALLOTASIS

Fig. 1-A   Fig 1-B

Measurement of bone mineral density. The knee joint was slightly flexed (Fig. 1-A) or the entire limb was raised (Fig. 1-B), so that the beam would pass parallel to the osteotomy. The limb was positioned by referring to the position of the fixators, which were determined on radiographs.
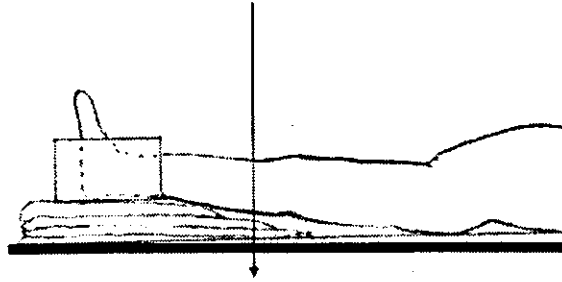
tube. Bone mineral density was expressed in grams per square centimeter. On the view obtained from the scan, we confirmed that the callus was visible without overlap of anterior or posterior cortical bone of the tibia, indicating that the beam was parallel to the osteotomy. Two regions of interest in each tibia were selected for measurement of regional bone mineral density with use of QDR for Windows software (version 11.2; Hologic). Following the previously described method with modification[9], we selected one region of interest within the distraction gap (Fig.1-C). The other was in the segment just distal to the distraction gap (Fig. 1-D). The region of interest in the distal segment was 8 mm in height and spanned the medial half of the tibia. The reproducibility error of the results was evaluated with three consecutive measurements and was found to be <3%. To test day-to-day reproducibility, a bone phantom (Hologic) was attached with a metal pin 5 cm above the bed, and its bone mineral density was measured daily for

one month. The coefficient of variation was 0.8%.

The bone mineral density of the callus was measured twice for each tibia: at the start of the consolidation period and four weeks after the start of the consolidation period. The first bone mineral density measurement was subtracted from the second to calculate the increase in bone mineral density over the four-week consolidation period.

Application of Ultrasound

For each patient, the limb to be treated with low-intensity pulsed ultrasound was randomly selected with use of a random-number generator on a computer. Ultrasound energy was provided by a Sonic Accelerated Fracture Healing System (SAFHS; Exogen, Piscataway, New Jersey). The treatment head module delivered an ultrasound signal composed of a burst width of 200 µsec containing 1.5-MHz sine waves, with a repetition rate of 1 kHz and a spatial average-temporal average
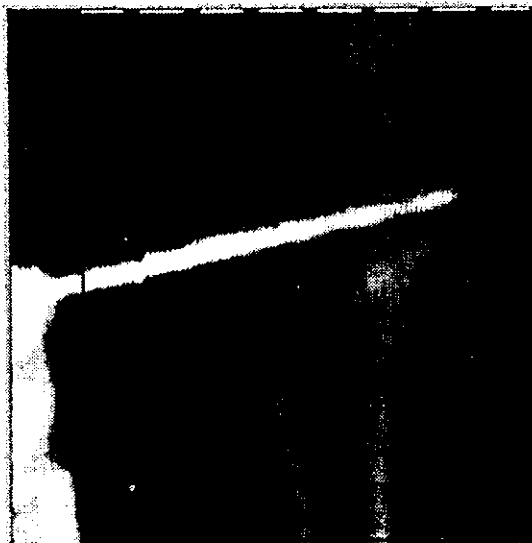

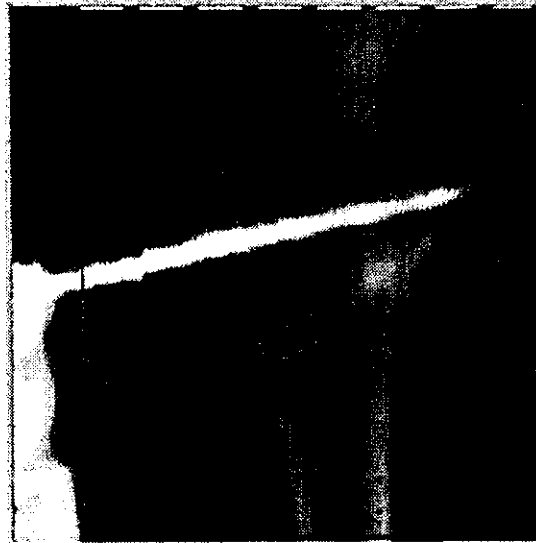Fig. 1-C   Fig. 1-D

Anteroposterior images produced by a dual-energy x-ray absorptiometry unit (QDR; Hologic) to measure bone mineral density in the proximal part of a tibia that underwent opening-wedge high tibial osteotomy. The regions of interest of measurement were set within the distraction gap (outlined in red) (Fig. 1-C) and the segment distal to the distraction gap (outlined in red) (Fig. 1-D).

intensity of 30 mW/cm². Within two days after the first bone mineral density measurement, we began daily twenty-minute ultrasound treatments on the one side, and we continued the treatment until the fixator was removed. The treatment head module was positioned on the anteromedial aspect of the proximal part of the leg at the level of the osteotomy and was fixed with a strap. All twenty-one patients were hospitalized until removal of the pins and were assisted by the hospital staff in carrying out the low-intensity pulsed ultrasound treatment.

Statistical Analysis

The t test was used to compare data between treated and untreated limbs. A p value of <0.05 was considered to indicate significance.

Results

Baseline Characteristics

None of the patients had previously undergone knee surgery such as meniscectomy or cruciate ligament repair. The mean weight of the patients was 61 ± 11 kg, and the mean body mass index was 26 ± 3. Three patients smoked during the treatment period.

Preoperatively, the femorotibial angle averaged 185° ± 5° in the ultrasound-treated limbs and 184° ± 5° in the controls, the range of knee flexion measured with manual goniometry averaged 121° ± 27° in the ultrasound-treated limbs and 125° ± 10° in the controls, and the range of knee extension averaged −4° ± 6° in the ultrasound-treated limbs and −3° ± 5° in the controls. Thus, the preoperative varus deformity and ranges of motion did not differ substantially between the ultrasound-treated and control limbs. Preoperatively, four patients had equal pain in the two knees, seven had more knee pain on the side that was later treated with low-intensity pulsed ultrasound, and ten patients had less pain on that side. The mean period of distraction did not differ between the ultrasound-treated tibiae (37 ± 7 days) and the control tibiae (37 ± 7 days). The distraction period was the same for both sides in eighteen patients. It was two days shorter on the ultrasound-treated side in one patient, four days shorter on the ultrasound-treated side in another patient, and three days shorter for the control limb in still another patient.

During the distraction period, patients experienced pain in the lower limbs and were occasionally unable to stand. After the start of the consolidation period, the pain decreased, and all patients walked using a pair of crutches. Pin-track infections developed in six limbs in the ultrasound-treated group and five limbs in the control group. These infections responded to local pin-site care and antibiotic treatment. We did not observe signs of infection at any osteotomy site or in any joint in the limbs.

As a result of randomization, the right limb was chosen for low-intensity pulsed ultrasound and the left limb served as the control in eleven patients. In ten patients, the left limb was chosen for low-intensity pulsed ultrasound and the right limb served as the control.
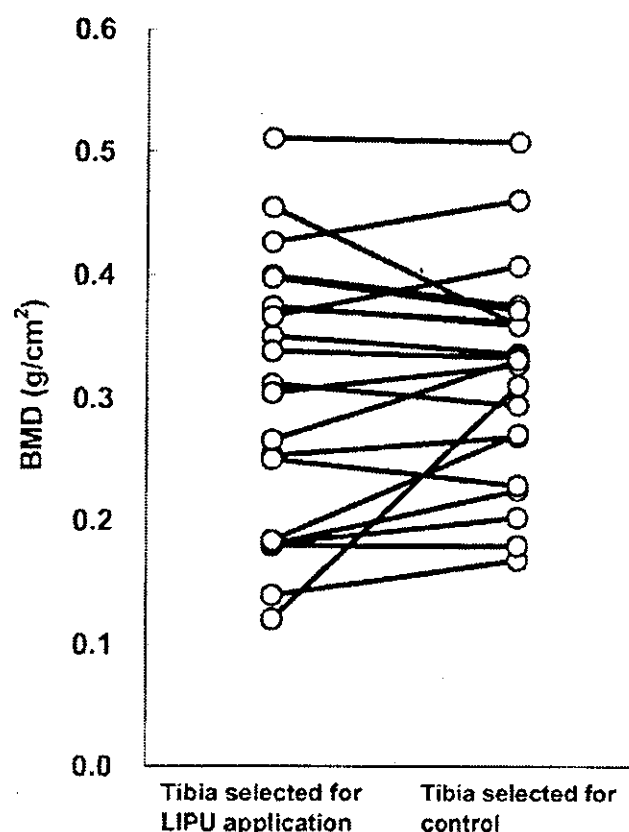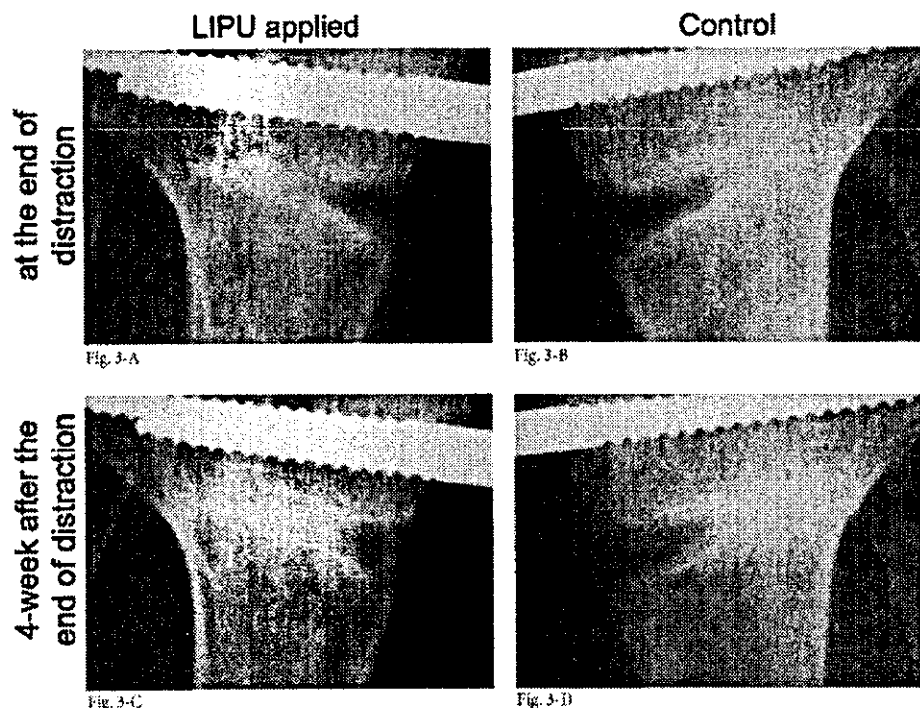

Fig. 2
Bone mineral density (BMD) of the distraction callus before the start of treatment with low-intensity pulsed ultrasound (LIPU). The tibiae selected for ultrasound treatment are shown on the left, and the control tibiae are shown on the right, with the values for the limbs of the same patient connected by lines. The mean bone mineral density was 0.30 ± 0.11 g/cm² in the tibiae selected for ultrasound treatment and 0.32 ± 0.09 g/cm² in control tibiae (p = 0.31, unpaired t test). Note that, in each patient, there was little difference in the callus bone mineral density between the two tibiae, whereas the callus bone mineral density varied more widely among individuals.

Bone Mineral Density

Before the start of the treatment with the low-intensity pulsed ultrasound, the bone mineral density of the distraction callus averaged 0.30 ± 0.11 g/cm² in the tibiae chosen to be treated with ultrasound and 0.32 ± 0.09 g/cm² in the controls (p = 0.31, unpaired t test) (Fig. 2). The mean increase in bone mineral density during the four-week treatment period was significantly greater in the ultrasound-treated tibiae (0.20 ± 0.12 g/cm²) than it was in the controls (0.13 ± 0.10 g/cm²) (p = 0.02, unpaired t test). In eighteen patients, the bone mineral density increased more in the ultrasound-treated limb than in the control limb; in three patients, the bone mineral density increased more in the control limb (Figs. 3-A through 4). Of the three patients who had a greater increase in the control limb, one was a smoker, two had had almost equal pain in the two knees, and one had had more knee pain

Figs. 3-A through 3-D Radiographs of a woman who underwent progressive opening-wedge osteotomy by hemicallotasis at the age of sixty-seven years. **Figs. 3-A and 3-B** Radiographs of the proximal parts of the right (Fig. 3-A) and left (Fig. 3-B) tibiae made at the end of distraction show that both limbs contained callus with moderate mineralization. After measurement of bone mineral density, low-intensity pulsed ultrasound (LIPU) was applied only to the right tibia; the left tibia was used as the control. **Figs. 3-C and 3-D** Four weeks later, the callus of the right tibia (Fig. 3-C) appears more consolidated than that of the left tibia (Fig. 3-D). The bone mineral density of the distraction gap was again measured after this four-week consolidation period. The increase in the bone mineral density in the callus was 0.29 g/cm³ in the right tibia and 0.10 g/cm³ in the left.

LIPU applied   Control

at the end of distraction

Fig. 3-A   Fig. 3-B

4-week after the end of distraction

Fig. 3-C   Fig. 3-D

in the ultrasound-treated limb than in the control limb.

The mean increase in bone mineral density in the segment just distal to the distraction gap during the four-week treatment period was 0.02 ± 0.09 g/cm³ in the ultrasound-treated tibiae and -0.03 ± 0.09 g/cm³ in the control tibiae. The difference between the two groups was not significant ($p = 0.07$).

Consolidation Period

The mean consolidation period was 7.1 ± 2.6 weeks (range, four to twelve weeks) in the ultrasound-treated group and 7.9 ± 2.4 weeks (range, five to thirteen weeks) in the control group. The consolidation period for the ultrasound-treated limb was shorter than that for the control limb in thirteen patients: it was three weeks shorter for four patients, two weeks shorter for four patients, and one week shorter for five patients. The consolidation period was the same on both sides in six patients, and, in two patients, consolidation occurred one week earlier in the control limb than in the ultrasound-treated limb. The fixators remained in place for a mean of 14.6 ± 3.0 weeks in the ultrasound-treated tibiae and for 15.5 ± 2.7 weeks in the controls.

Discussion

Bone-forming activity varies among individuals[9]. This variation may account in part for the difficulties in determining the effects of low-intensity pulsed ultrasound in clinical studies with limited numbers of patients. In the present study, the same surgical procedure was performed on both tibiae of each patient on the same day. Low-intensity pulsed ultrasound was applied on one side, whereas the contralateral side
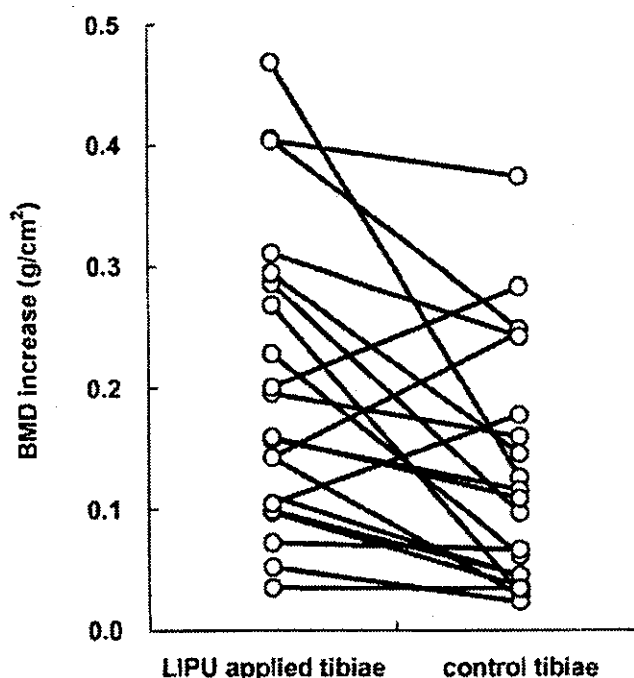
Fig. 4
Increases in callus bone mineral density (BMD) during the four-week consolidation period in the limbs treated with low-intensity pulsed ultrasound (LIPU) (left) and the control limbs (right), with the values for the limbs of the same patient connected by lines. The mean increase in bone mineral density was 0.20 ± 0.12 g/cm³ in the ultrasound-treated tibiae and 0.13 ± 0.10 g/cm³ in the control tibiae ($p = 0.02$, unpaired t test).

was used as the internal control. Before the treatment with the low-intensity pulsed ultrasound, the mean difference in callus bone mineral density between the left and right limbs of the same patient was usually relatively small, whereas the callus bone mineral density varied more substantially among individuals (Fig. 2). The increase in bone mineral density during the four-week consolidation period also varied among individuals, suggesting variation in bone-forming activities among patients.

The present study showed that low-intensity pulsed ultrasound significantly enhances the increase in mineralization of the callus during hemicallotasis, as assessed by measuring bone mineral density. In fact, the external fixators were removed an average of one week earlier from the ultrasound-treated limbs than from the control limbs. In the present study, low-intensity pulsed ultrasound was applied after distraction had ceased, in order to assess the bone mineral density of the distraction callus before the ultrasound treatment. A recent investigation of rabbits showed that low-intensity pulsed ultrasound stimulates bone formation most effectively during the distraction phase. Future clinical studies should address the question of whether additional low-intensity pulsed ultrasound treatment during the distraction phase can further shorten the period necessary for callus maturation.

The effects of low-intensity pulsed ultrasound on maturation of distraction callus have been investigated in several animal studies, with controversial results. In a rabbit study, Shimazaki et al. found that bone mineral density, hard callus area, and mechanical test scores were greater in distraction callus treated with low-intensity pulsed ultrasound than in the control group. In a study of rats, Eberson et al. found that radiographically assessed healing occurred earlier in ultrasound-treated bones than in control bones and that bone volume fraction and trabecular bone pattern factor were higher in the ultrasound-treated bones. In a study of rabbits, Tis et al. found a greater hard callus area and less fibrous tissue in bones treated with low-intensity pulsed ultrasound than in control bones. Neither Eberson et al. nor Tis et al. found a difference in bone mineral density or mechanical strength of distraction callus between ultrasound-treated bones and controls, although Eberson et al. observed a trend toward greater mechanical strength in ultrasound-treated bones. Uglow et al. found no substantial difference in bone mineral content, cross-sectional area, or strength of distraction callus between ultrasound-treated bones and control bones of rabbits. In all of the animal studies mentioned above, osteotomy and distraction were performed at the diaphysis, which consists of thick cortical bone. In the metaphyseal segment adjacent to the distraction callus in the present study, the bone mineral density tended to increase more in the ultrasound-treated limbs than in the control limbs, although the difference was not significant (p = 0.07). Uglow et al. found no significant difference in the reduction of volumetric bone mineral density of the segment adjacent to the distraction callus in the diaphysis between their ultrasound-treated group and control group (p > 0.5) in rabbits. Although the applicability of findings of animal studies to human clinical research remains unclear, results obtained from the present study and those of animal studies collectively suggest that metaphyseal trabecular bone might be more susceptible than diaphyseal cortical bone to mechanical forces inherent to low-intensity pulsed ultrasound.

In vitro and in vivo studies have been performed to investigate the mechanisms by which mechanical stimulation due to low-intensity pulsed ultrasound is translated into a biological response. Low-intensity pulsed ultrasound has effects on chondrocytes as well as osteoblasts. Rawool et al. reported that low-intensity pulsed ultrasound also stimulates angiogenesis, thus increasing local blood flow. The usefulness of low-intensity pulsed ultrasound in fracture-healing has previously been established. Distraction osteogenesis may involve an ossification process (transchondroid ossification) different from that of fracture-healing. Future studies should include clarification of the distraction osteogenesis-specific mechanism that translates mechanical forces due to low-intensity pulsed ultrasound into bone formation. ∎

Noriyuki Tsumaki, MD
Takahiro Ochi, MD
Hideki Yoshikawa, MD
Department of Orthopaedics, Osaka University Graduate School of Medicine, 2-2 Yamadaoka, Suita, Osaka 565-0871, Japan. E-mail address for N. Tsumaki: tsumaki-n@umin.ac.jp

Masaaki Kakiuchi, MD
Jiro Sasaki
Departments of Orthopaedic Surgery (M.K.) and Radiology (J.S.), Osaka Police Hospital, 10-31 Kitayama-cho, Tennoji-ku, Osaka 543-0035, Japan

References

1. **Wolff J.** The law of bone remodelling. New York: Springer; 1986.

2. **Huiskes R, Ruimerman R, van Lenthe GH, Janssen JD.** Effects of mechanical forces on maintenance and adaptation of form in trabecular bone. Nature. 2000;405:704-6.

3. **Yang KH, Park SJ.** Stimulation of fracture healing in a canine ulna full-defect model by low-intensity pulsed ultrasound. Yonsei Med J. 2001;42:503-8.

4. **Yang KH, Parvizi J, Wang SJ, Lewallen DG, Kinnick RR, Greenleaf JF, Bolander ME.** Exposure to low-intensity ultrasound increases aggrecan gene expression in a rat femur fracture model. J Orthop Res. 1996;14:802-9.

5. **Rubin C, Bolander M, Ryaby JP, Hadjiargyrou M.** The use of low-intensity ultrasound to accelerate the healing of fractures. J Bone Joint Surg Am. 2001;83:259-70.